NASA CR-54725
SRI - TN - 8

ONE-DIMENSIONAL ANALYSIS OF THE HYPERVELOCITY IMPACT OF A PELLET ONTO A THIN BUMPER

by

P.S. GOUGH

prepared for

NATIONAL AERONAUTICS AND SPACE ADMINISTRATION

CONTRACT NAS 3-10299

SPACE RESEARCH INSTITUTE (QUEBEC) INC.
MONTREAL, CANADA

NASA CR-54725
SRI - TN - 8

TOPICAL REPORT

ONE-DIMENSIONAL ANALYSIS OF THE HYPERVELOCITY IMPACT OF A PELLET ONTO A THIN BUMPER

by

P.S. Gough

prepared for

NATIONAL AERONAUTICS AND SPACE ADMINISTRATION

November 1967

CONTRACT NAS3-10299

Technical Management
NASA Lewis Research Center
Cleveland, Ohio
Liquid Rocket Technology Branch
Gordon T. Smith

SPACE RESEARCH INSTITUTE (QUEBEC) INCORPORATED
892 Sherbrooke Street West
Montreal 2, Quebec, Canada

SUMMARY

A one-dimensional hydrodynamic formulation of the hypervelocity impact of a pellet onto a thin bumper has been analyzed by finite difference techniques. A first order scheme due to Lelevier was used together with the well-known artificial viscosity due to Von Neumann and Richtmyer. Studies were made assuming a perfect gas equation of state and results for the complete interaction including the effect of a secondary surface are presented here.

The finite difference code was found to remain computationally stable throughout all phases of the investigation. However, the long term expansion results are not within the realm of the physical assumption of one-dimensionality. Consequently, the long term stability is more important mathematically than physically. A useful feature of the present work is the elimination of small local disturbances or "jitters" which often accompany the use of artificial viscosities. A technique of smoothing, which does not appear to have been used before on this type of problem, was successfully employed.

FOREWORD

The results presented in this report constitute part of an overall theoretical research program on the hypervelocity impact of pellets on thin bumper plates. The work is sponsored by the Lewis Research Center of the National Aeronautics and Space Administration under Contracts NAS3-7946 and NAS3-10299. The technical monitor is Mr. Gordon T. Smith.

The author wishes to express his gratitude to Dr. G.G. Bach and Dr. J.H. Lee who suggested the problem and approach. The assistance and constructive criticisms of N. Chepurniy, W.H. Friend, and W.A. Watkins are acknowledged. Thanks are also due to Dr. S.A. Gordon for his valuable criticisms during the writing of this report. The important role played by Dr. G.V. Bull, director of the Space Research Institute, in the initiation of this study is also appreciated.

TABLE OF CONTENTS

LIST OF FIGURES

NOMENCLATURE

1. Symbols used repeatedly in the text.

a	$a = l_v / \Delta x$
C	contact surface
c	isentropic sound speed
D	shock velocity
$\mathcal{E}$	internal energy density
F	$\mathcal{E} = F(P, \rho)$
l_v	coefficient of artificial viscosity
l_p	pellet to bumper length ratio
p	pressure
q	artificial viscosity
$\overleftarrow{\mathcal{R}}_B, \overrightarrow{\mathcal{R}}_p$	bumper and pellet rarefactions
$\overrightarrow{S}_B, \overleftarrow{S}_P$	bumper and pellet shocks respectively
t	time
u	velocity
V	pellet impact velocity in bumper frame
W_p, W_B	shock velocities (of $\overleftarrow{S}_p$, $\overrightarrow{S}_B$ respectively)
x	axial coordinate
γ	polytropic gas constant
δ	time increment associated with initialization of $\overleftarrow{\mathcal{R}}_B, \overrightarrow{\mathcal{R}}_p$
Δ	thickness of transition zone shock wave when artificial viscosity is present
$\Delta x, \Delta t$	space - time mesh size
μ^2	$\dfrac{\gamma - 1}{\gamma + 1}$

ν	smoothing element index
ξ, φ	dummy variables
ρ	density

2. Symbols used repeatedly in the Appendices

A	$1 + ul\ (e^{-ik\Delta x} - 1)$
B	$\sin(k\Delta x)$
G	amplification matrix
I	identity matrix
k	Fourier wave number
O	$f(t) = O(\Delta t) \Rightarrow \lim\limits_{\Delta t \to 0} \frac{f(t)}{\Delta t} = \text{finite}$
λ	eigenvalue of G

INTRODUCTION

This report is one in a continuing series of studies of the protection of a spacecraft in a meteoroid environment. The method of protection is due to Whipple. Consider Fig. 0.1. The spacecraft hull is surrounded by a thin shell or "bumper". The high kinetic energy of an impinging meteoroid may be expected to vaporize both the meteoroid and a local section of the bumper. The expansion of the resulting gas cloud will then disperse the original meteoroid momentum over a large section of the inner hull. In this way a considerable reduction of pressure on the hull may be expected. The reduction will depend, among other things, on the spacing between the bumper and the hull.

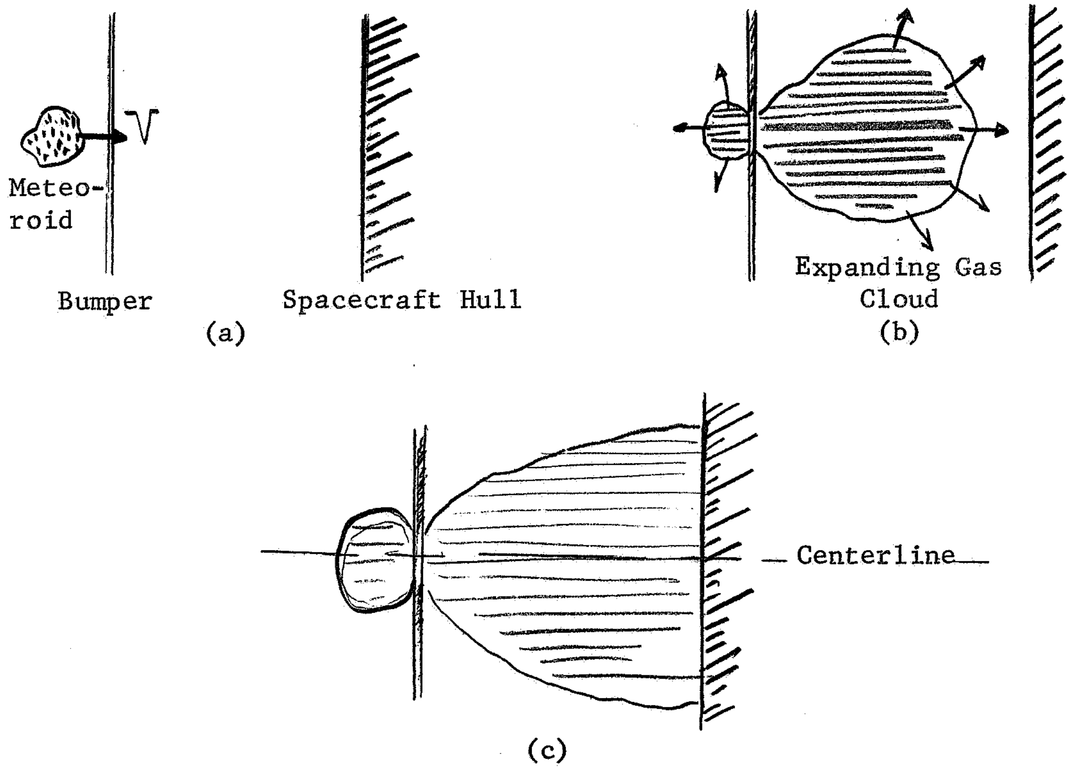

Schematic of Meteoroid-Bumper Interaction

Fig. 0.1

A fundamental assumption in the foregoing is that the kinetic energy will be high enough to produce vaporization. For most materials (sand, clay, granite, aluminum, steel) the vaporization energy is of the order of 10^{10} to 10^{12} ergs/grams. Hence velocities in excess of 10 km/sec should produce vaporization. At the high meteoroid impact velocities of 30 km/sec the assumption that vaporization takes place should certainly be valid.

As an experimental simulation of the physical situation, one may project a cylindrical pellet to impact normally on a thin sheet. A cylindrical pellet is used to obtain rotational symmetry about the direction of the impact velocity. Fig. 0.2 shows high speed photographs of a cylindrical Lexan pellet that has been accelerated by a light gas gun impacting on a lead sheet. Frames 1-4 show the approach and destruction of the pellet while frames 5-8 show the expansion of the resulting gas cloud.

As a preliminary to attempting an analysis of the flow represented in Fig. 0.2 we have studied a one-dimensional approximation. The approach taken is that initiated by Dr. G.V. Bull (Ref. 1). A hydrodynamic model is proposed and the kinetic energy assumed sufficiently high that vaporization energy may be ignored. Plasma effects due to the stripping of outer orbital electrons may then become important. However such effects are not considered in this report.

The model we have adopted is one-dimensional in that radial effects are ignored. Such an assumption can only be valid for short times after impact. If we interpret the study made in this report as applying to the centerline [Fig. 0.1(c)], then by a short time we mean a time sufficient for radial attenuation waves to penetrate to the center. We

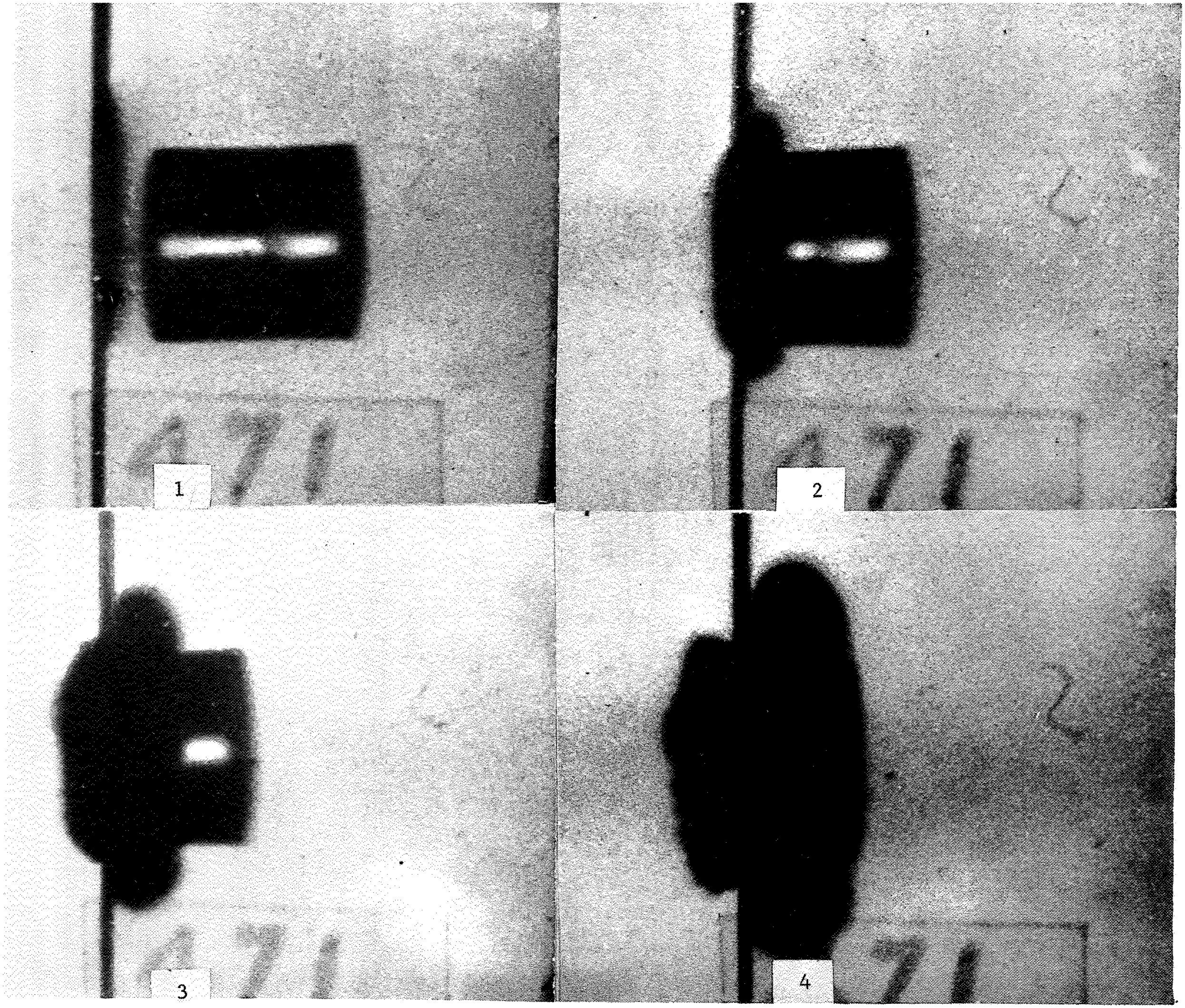

Fig. 0.2 B & W 300 Framing Camera Sequence of Shot 471:
A 12.7 mm diameter x 12.7 mm long Lexan projectile
and a 0.51 mm thick lead wall. Impact velocity 6.04 km/sec.

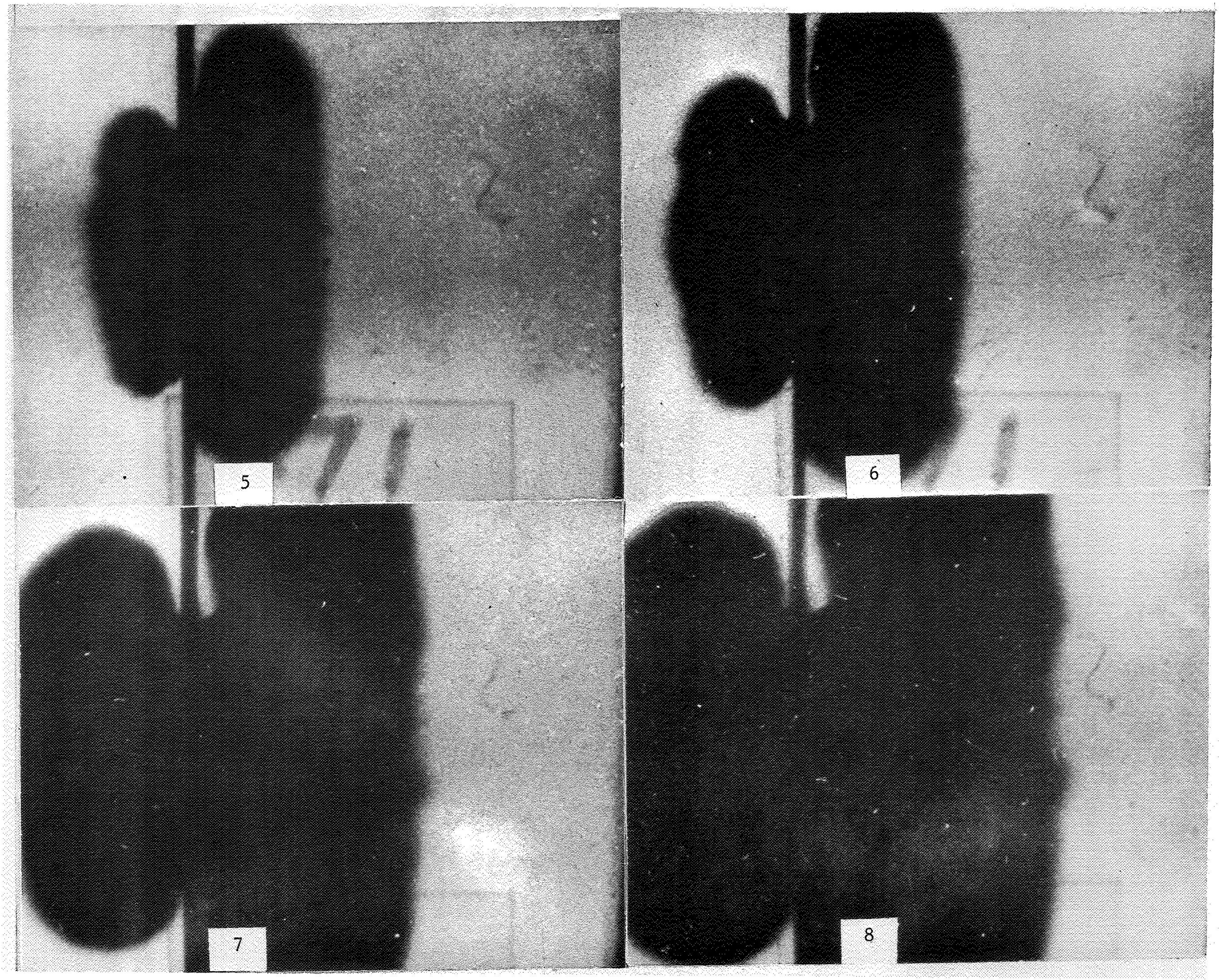

Fig. 0.2 (Continued)

might anticipate that the one-dimensional model is valid during the period in which the pellet is being vaporized. This will be so if the length of the pellet is small compared to the radius. It is useful to visualize the one-dimensional model as describing the impact of one infinite flat plate onto another.

The limitations of the assumption of one-dimensionality make it difficult to obtain experimental confirmation of the results contained in this report. Also, the upper limit of the experimental velocity range is roughly 10 km/sec, which is well below meteoroid velocities. Thus, while we may expect vaporization to occur, it does not appear reasonable to ignore the binding energy in comparison with the kinetic energy corresponding to such a velocity. Experimental confirmation is, therefore, further hampered by the need to include the effects of non-negligible vaporization energy.

Since the one-dimensional approach has reasonable validity during the vaporization of the pellet, we are able to study the "destruction potential" of the bumper. The shock moving into the pellet will eventually be overtaken by a release wave from the free surface of the bumper, provided the pellet is sufficiently long. The high pressure behind the pellet shock will consequently decay. Eventually it will reach some critical level at which insufficient energy is available for vaporization. Although vaporization energy was neglected and an ideal gas equation used in the present study, it was possible to decide <u>a posteriori</u> to what degree an impinging pellet would have been destroyed.

It was to be expected that the long term expansion profiles would produce pressures and densities well in excess of experimental values as no mechanism for radial decay could be involved in the one-dimensional model. Nonetheless, a calculation of pressures at a secondary surface downstream of the impact point was performed to determine whether qualitative agreement could be obtained, with the experimental conclusion that the maximum pressure at a secondary surface is not much higher than the maximum total pressure at the same point in undisturbed flow.

An important concern of this report has been the development of a successful finite difference code. In this regard two features appear. The code we have developed was found to remain computationally stable throughout all stages of the analysis. Secondly the rather annoying problem of "jitters", or pseudo-shocks, which often accompany an artificial dissipation term have been eliminated. We borrowed a technique familiar to meteorologists but which does not seem to have been used in this connection until now. This technique is one of designing a "smoother" or filter which deletes any small disturbance whose wavelength is of the order of the grid interval. Judiciously applied, a smoother not only removes "jitters" but also enhances the stability of the finite difference program.

CHAPTER ONE

1.1 The Initial States

The model we adopt to describe the impact process is due to Bull (Ref. 1). We consider the normal impact of a moving plate (the pellet) onto one at rest in the laboratory system of coordinates (the bumper). At the moment of impact strong shock waves are produced which propagate through the pellet and bumper, decelerating the former and accelerating the latter. In the shocked regions high thermodynamic energies will be produced at the expense of the pellet kinetic energy. It is assumed that the kinetic energy involved is sufficiently high that the resulting thermodynamic energy will be large compared with the intermolecular binding forces of the pellet and bumper materials. At the same time plasma effects are ignored and the hydrodynamic equations presumed to apply throughout the pellet and bumper materials.

In terms of the fluid descriptions of Ref. 1, we represent the situation shortly after impact in Fig. 1.1 below.

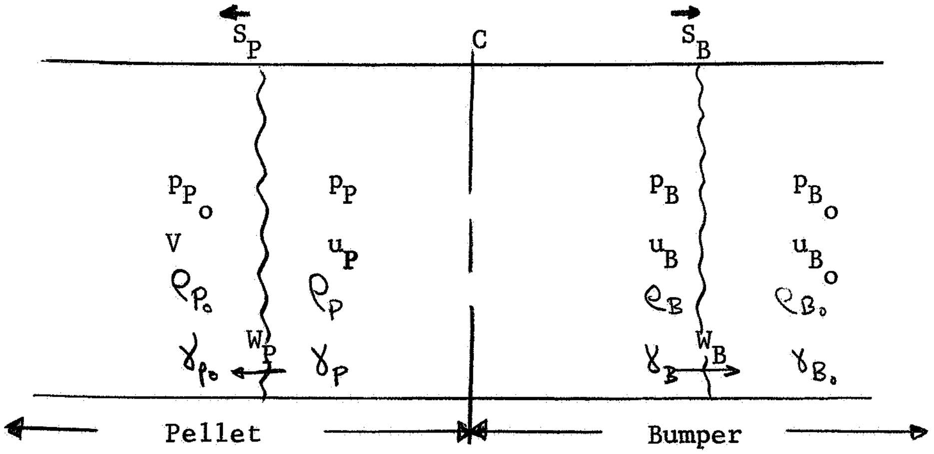

Fig. 1.1

Initial States after Impact

We assume that the fluids obey a polytropic gas law with exponent γ. Pressure, density and velocity have been denoted by p, ρ, u respectively. The subscripts B and P refer to bumper and pellet media respectively. The further subscript o has been used to denote initial or unshocked states. A contact front C is presumed to separate the pellet from the bumper material at all times. $\overleftarrow{S}_p$ and $\overrightarrow{S}_B$ denote the shocks moving into pellet and bumper materials with respective velocities W_p, W_B relative to the unshocked bumper.

Under the assumptions that

(i) $\overleftarrow{S}_p$, $\overrightarrow{S}_B$ are strong shocks;

(ii) vaporization energy is negligible; and

(iii) the bumper and pellet gases obey a perfect gas law;

one may use the Rankine-Hugoniot relations together with continuity of pressure and particle velocity across the contact front, to obtain (Ref. 1):

$$\frac{u_B}{V} = \frac{1}{1 + \sqrt{\frac{\gamma_B + 1}{\gamma_p + 1} \; \rho_{B_o}/\rho_{p_o}}} \quad ; \quad u_p = u_B \qquad 1.1.1$$

$$\rho_B = \frac{\gamma_B + 1}{\gamma_B - 1} \rho_{B_o} \quad ; \quad \rho_p = \frac{\gamma_p + 1}{\gamma_p - 1} \rho_{p_o} \qquad 1.1.2$$

$$W_B = \frac{\gamma_B + 1}{2} u_B \quad ; \quad W_p = \frac{\gamma_p + 1}{2} u_p - \frac{\gamma - 1}{2} V \qquad 1.1.3$$

$$p_p = p_B = \frac{\gamma_B + 1}{2} \; \frac{\rho_{B_o} V^2}{\left(1 + \sqrt{\frac{\gamma_B + 1}{\gamma_p + 1} \; \frac{\rho_{B_o}}{\rho_{p_o}}} \right)^2} \qquad 1.1.4$$

We now non-dimensionalize as follows:

$$\left.\begin{array}{l} \rho \longrightarrow \rho/\rho_{B_o} \\ p \longrightarrow p/\rho_{B_o}V^2 \\ u \longrightarrow u/V \end{array}\right\} \qquad 1.1.5$$

We choose as our unit of length the bumper thickness. Consequently the unit of time is given by (Bumper Thickness)/(Impact Velocity of Pellet)

$$\text{time} \longrightarrow \text{time} \times \frac{\text{Impact Velocity of Pellet}}{\text{Bumper thickness}} \qquad 1.1.6$$

We fix our coordinate system by choosing the origin of the x-axis at the contact front at the instant of impact (t = o).

Equations (1.1.1) to (1.1.4) determine the shocked fluid properties until such time as $\overleftarrow{S}_p$ or $\overrightarrow{S}_B$ encounters a free surface. We assume that the impact process takes place in a vacuum and that $\overrightarrow{S}_B$ reaches the downstream bumper surface before $\overleftarrow{S}_p$ reaches the upstream pellet surface. From (1.1.3) and (1.1.6), the non-dimensional time at which $\overrightarrow{S}_B$ reaches the downstream bumper free surface is given by:

$$t_o = \frac{2}{(\gamma_B + 1)\, u_B}$$

i.e.

$$t_o = \frac{2}{\gamma_B + 1}\left\{1 + \sqrt{\frac{\gamma_B + 1}{\gamma_p + 1}\,\frac{\rho_{B_o}}{\rho_{P_o}}}\right\} \qquad 1.1.7$$

At time t_o the contact front C will be located at:

$$x_c = u_B t_o = \frac{2}{\gamma_B + 1} \qquad 1.1.8$$

The pellet shock will be at:

$$x_{sp} = W_p t_o$$

$$x_{sp} = \frac{\gamma_p + 1}{\gamma_B + 1} - \frac{\gamma_p - 1}{\gamma_B + 1}\left\{ 1 + \sqrt{\frac{\gamma_B + 1}{\gamma_p + 1}\,\frac{\rho_{B_o}}{\rho_{P_o}}} \right\} \qquad 1.1.9$$

Consequently, at the instant when $\vec{S}_B$ reaches the downstream bumper free surface, the shocked fluid profiles are given by:

$$u(x,t_o) = \frac{1}{1 + \sqrt{\frac{\gamma_B + 1}{\gamma_p + 1}\,\frac{\rho_{B_o}}{\rho_{P_o}}}} \qquad x_{sp} \leq x \leq 1 \qquad 1.1.10$$

$$p(x,t_o) = \frac{\gamma_B + 1}{2}\,\frac{1}{\left(1+\sqrt{\frac{\gamma_B + 1}{\gamma_p + 1}\,\frac{\rho_{B_o}}{\rho_{P_o}}} \right)^2} \qquad x_{sp} \leq x \leq 1 \qquad 1.1.11$$

$$\rho\,(x,t_o) = \frac{\gamma_p + 1}{\gamma_p - 1}\,\left(\rho_{P_o}/\rho_{B_o} \right) \qquad x_{sp} \leq x \leq x_c \qquad 1.1.12$$

$$\rho\,(x,t_o) = \frac{\gamma_B + 1}{\gamma_B - 1} \qquad x_c \leq x \leq 1 \qquad 1.1.13$$

If we take the pellet length to be l_p (in units of bumper thickness), then at t_o the upstream pellet free surface will be located at:

$$x_p = - l_p + t_o$$

$$x_p = -l_p + \frac{2}{\gamma_B + 1}\left\{ 1 + \sqrt{\frac{\gamma_B + 1}{\gamma_p + 1}\,\frac{\rho_{B_o}}{\rho_{P_o}}} \right\} \qquad 1.1.14$$

Then the unshocked fluid profiles are given by:

$$u(x,t_o) = 1 \qquad x_p \leq x \leq x_{sp} \qquad 1.1.15$$

$$p(x,t_o) = 0 \qquad x_p \leq x \leq x_{sp} \qquad 1.1.16$$

$$\rho(x,t_o) = \rho_{P_o}/\rho_{B_o} \qquad x_p \leq x \leq x_{sp} \qquad 1.1.17$$

The condition that $\overrightarrow{S}_B$ reach the downstream bumper free surface while $\overleftarrow{S}_p$ is still in motion can be written:

$$x_p < x_{sp}$$

or
$$-1_p + \frac{2}{\gamma_B + 1}\left\{1 + \sqrt{\frac{\gamma_B + 1}{\gamma_p + 1}\,\frac{\rho_{B_o}}{\rho_{P_o}}}\right\} < \frac{\gamma_p + 1}{\gamma_B + 1}$$
$$- \frac{\gamma_p - 1}{\gamma_B + 1}\left\{1 + \sqrt{\frac{\gamma_B + 1}{\gamma_p + 1}\,\frac{\rho_{B_o}}{\rho_{P_o}}}\right\}$$

i.e.
$$1_p > \frac{\gamma_p + 1}{\gamma_B + 1}\sqrt{\frac{\gamma_B + 1}{\gamma_p + 1}\,\frac{\rho_{B_o}}{\rho_{P_o}}} \qquad 1.1.18$$

1.2 The Expansion States

Having determined the initial shocked states we turn to the question of the expansion process. Consider Fig. 1.2.

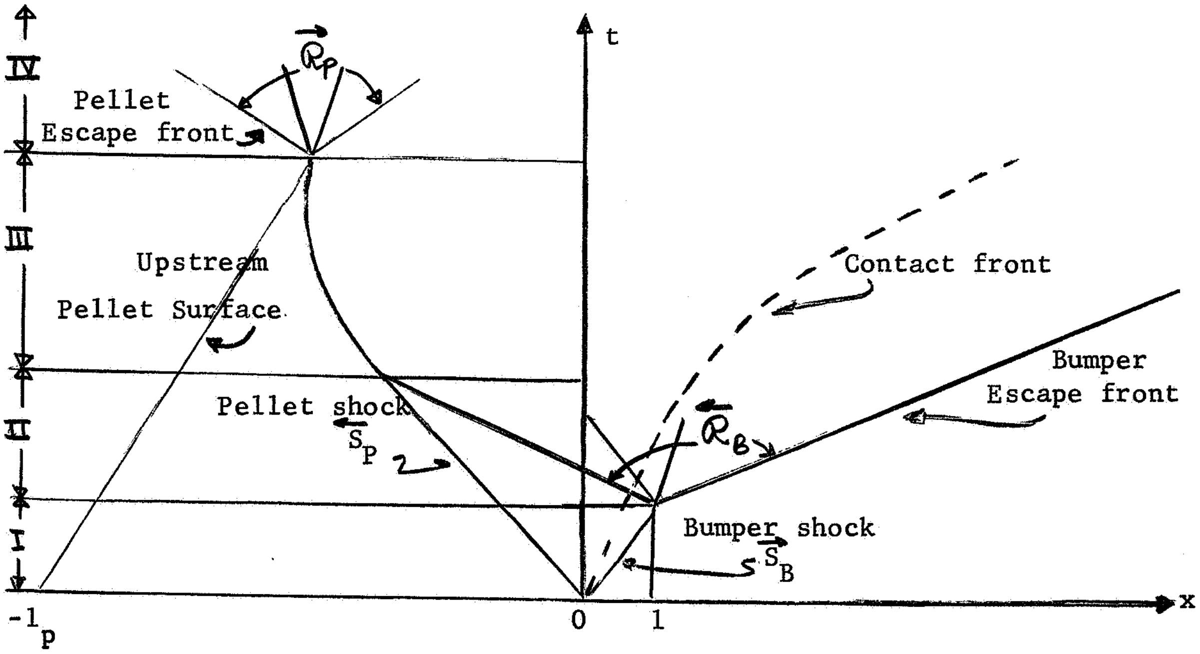

Wave Diagram of Impact Process

Fig. 1.2

We may divide the flow into four characteristically different periods. In period I both shocks are progressing with undiminished strength. The profiles during this period are given by (1.1.10) to (1.1.13) and (1.1.15) to (1.1.17). In period II, $\overrightarrow{S}_B$ has reached the downstream bumper free surface and generated a rarefaction $\overleftarrow{\mathcal{R}}_B$. As $\overleftarrow{\mathcal{R}}_B$ does not overtake $\overleftarrow{S}_p$ during this period, the flow is isentropic in each zone of shocked or unshocked fluid. In period III, $\overleftarrow{\mathcal{R}}_B$ has overtaken $\overleftarrow{S}_p$ before the latter has reached the upstream pellet free surface. Evidently period III may or may not occur. However, the resulting shock decay is of primary interest in this report and it will be assumed that period III does occur. Due to the decay of $\overleftarrow{S}_p$ in period III, the governing equations will not be isentropic. In period IV, $\overleftarrow{S}_p$ has generated the pellet rarefaction $\overrightarrow{\mathcal{R}}_p$. The governing equations will be isentropic or non-isentropic depending on whether or not period III (i.e. shock decay) has occurred.

In the case that we are dealing with a like material impact, one can write a simple solution for the flow in period II (Ref. 4, 5). $\overleftarrow{\mathcal{R}}_B$ is characterized by two surfaces. An expansion front moves back into the gas relaxing the highly shocked states created in period I, while an escape front moves into the ambient vacuum at constant velocity. The solution we write down is valid as long as the expansion front progresses through a homogeneous region in which the flow properties are constant. Consequently, in the case of unlike material impacts, the solution will be valid until the expansion front overtakes the contact surface.

Let the constant particle velocity and sound speed at the expansion front be u_o and c_o respectively. Then the expansion front moves according to:

$$(x - x_o) = (u_o - c_o)(t - t_o) \tag{1.2.1}$$

where x_o is the initial position of the bumper free surface ($x_o = 1$ in non-dimensional units) and t_o is the time at which $\mathcal{R}_B$ is generated [see equation (1.1.7)]. The escape front is found to move according to

$$(x - x_o) = (\frac{2}{\gamma - 1} c_o + u_o)(t - t_o) \tag{1.2.2}$$

The governing equations are isentropic and are found to have the solution (Refs. 4, 5):

$$c(x, t) = \frac{\gamma - 1}{\gamma + 1} \left\{ u_o - \frac{(x - x_o)}{(t - t_o)} \right\} + \frac{2c_o}{\gamma + 1} \tag{1.2.3}$$

$$u(x, t) = \frac{2}{\gamma + 1} \left\{ \frac{x - x_o}{t - t_o} + c_o \right\} + \frac{\gamma - 1}{\gamma + 1} u_o \tag{1.2.4}$$

valid between the extremes defined by (1.2.1) and (1.2.2).

1.3 Finite Difference Representation of the Isentropic Equations

In the case that one is dealing with unlike materials or if period III (Fig. 1.2) does not occur, it is convenient to have a finite difference scheme for the isentropic equations. The results of Section 1.2 may be used to eliminate the initial discontinuities at free surfaces and to produce smooth initial distributions.

One may write the isentropic equations as:

$$\frac{2}{\gamma - 1} \frac{\partial c}{\partial t} + c \frac{\partial u}{\partial x} + \frac{2u}{\gamma - 1} \frac{\partial c}{\partial x} = 0 \tag{1.3.1}$$

$$\frac{\partial u}{\partial t} + u \frac{\partial u}{\partial x} + \frac{2c}{\gamma - 1} \frac{\partial c}{\partial x} = 0 \tag{1.3.2}$$

We represent the various derivatives in the form:

$$\frac{\partial \xi}{\partial x}(x,t) = \frac{1}{2\Delta x}\left\{ \xi(x+\Delta x,t) - \xi(x-\Delta x,t)\right\} \qquad 1.3.3$$

$$\frac{\partial \xi}{\partial t}(x,t) = \frac{1}{\Delta t}\left\{ \xi(x,t+\Delta t) - \frac{1}{2}\left(\xi(x+\Delta x,t) + \xi(x-\Delta x,t)\right)\right\} \qquad 1.3.4$$

where $\xi(x,t)$ is some variable of x and t and the symbols Δx, Δt represent intervals in the space-time mesh.

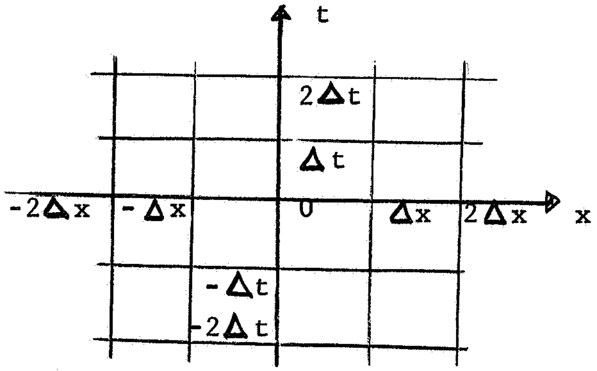

Finite Difference Grid

Fig. 1.3

The situation is indicated in Fig. 1.3. Information concerning field variables is known at the grid points $(j\Delta x, n\Delta t)$ where n, j are integers. For convenience we write

$$\xi_j^n = \xi(j\Delta x, n\Delta t)$$

so that (1.3.3), (1.3.4) may be written

$$\frac{\partial \xi_j^n}{\partial x} = \frac{1}{2\Delta x}\left(\xi_{j+1}^n - \xi_{j-1}^n\right)$$

$$\frac{\partial \xi_j^n}{\partial t} = \frac{1}{\Delta t}\left(\xi_j^{n+1} - \frac{1}{2}\left(\xi_{j+1}^n + \xi_{j-1}^n\right)\right)$$

Substitution of these representations into (1.3.1), (1.3.2) yields, after rearrangement:

$$c_j^{n+1} = \frac{1}{2}\left(c_{j+1}^n + c_{j-1}^n \right) - \frac{\gamma - 1}{2} \frac{\Delta t}{\Delta x} \left(c_j^n \frac{u_{j+1}^n - u_{j-1}^n}{2} \right.$$

$$\left. + \frac{2u_j^n}{\gamma - 1} \frac{c_{j+1}^n - c_{j-1}^n}{2} \right) \qquad 1.3.5$$

$$u_j^{n+1} = \frac{1}{2}\left(u_{j+1}^n + u_{j-1}^n \right) - \frac{\Delta t}{\Delta x} \left(u_j^n \frac{u_{j+1}^n - u_{j-1}^n}{2} \right.$$

$$\left. + \frac{2c_j^n}{\gamma - 1} \frac{c_{j+1}^n - c_{j-1}^n}{2} \right) \qquad 1.3.6$$

Equations (1.3.5), (1.3.6) are the working form of the finite difference scheme. The right hand side contains only information at time $n \Delta t$. This information is used to predict the values of u and c at each grid point $j \Delta x$ at time $(n + 1)\Delta t$. One may show, however, that (1.3.5), (1.3.6) will produce solutions closely approximating those of (1.3.1), (1.3.2) only under the restriction that

$$\frac{\Delta t}{\Delta x} (u \pm c) < 1 \qquad 1.3.7$$

Equation (1.3.7) is referred to as the stability condition for the finite difference scheme (1.3.5), (1.3.6) and is derived in Appendix A.

The treatment of boundaries is discussed in Section 1.7.

1.4 Finite Difference Representation of the Non-Isentropic Equations

One has, for the conservation of mass, momentum and energy:

$$\frac{\partial \rho}{\partial t} + u \frac{\partial \rho}{\partial x} + \frac{\rho \partial u}{\partial x} = 0 \qquad 1.4.1$$

$$\frac{\partial u}{\partial t} + u\frac{\partial u}{\partial x} + \frac{1}{\rho}\frac{\partial p}{\partial x} = 0 \qquad 1.4.2$$

$$\frac{\partial \mathcal{E}}{\partial t} + u\frac{\partial \mathcal{E}}{\partial x} + \frac{p}{\rho}\frac{\partial u}{\partial x} = 0 \qquad 1.4.3$$

together with the equation of state:

$$\mathcal{E} = F(p, \rho) \qquad 1.4.4$$

One may form three simple representations for the first derivative:

$$\frac{\partial \xi}{\partial x} \simeq \frac{1}{\Delta x}\left(\xi(x + \Delta x) - \xi(x)\right) \qquad \text{(Forward Difference)}$$

$$\frac{\partial \xi}{\partial x} \simeq \frac{1}{\Delta x}\left(\xi(x) - \xi(x - \Delta x)\right) \qquad \text{(Backward Difference)}$$

$$\frac{\partial \xi}{\partial x} \simeq \frac{1}{2\Delta x}\left(\xi(x + \Delta x) - \xi(x - \Delta x)\right)$$

(Centered Difference)

The substitution of centered differences for the spatial derivatives in (1.4.1) to (1.4.3) produces a scheme which is unconditionally unstable (Ref. 7). Consequently we use the first order scheme due to Lelevier:

$$\frac{\rho_j^{n+1} - \rho_j^n}{\Delta t} + u_j^{n+1}\frac{\rho_j^n - \rho_{j-1}^n}{\Delta x} = -\rho_j^n\frac{u_{j+1}^{n+1} - u_{j-1}^{n+1}}{2\Delta x},$$

$$u_j^{n+1} \geq 0 \qquad 1.4.5$$

$$\frac{u_j^{n+1} - u_j^n}{\Delta t} + u_j^n\frac{u_j^n - u_{j-1}^n}{\Delta x} = -\frac{1}{\rho_j^n}\frac{p_{j+1}^n - p_{j-1}^n}{2\Delta x},$$

$$u_j^n \geq 0 \qquad 1.4.6$$

$$\frac{\varepsilon_j^{n+1} - \varepsilon_j^{n}}{\Delta t} + u_j^{n+1}\,\frac{\varepsilon_j^{n} - \varepsilon_{j-1}^{n}}{\Delta x} = \frac{-p_j^{n}}{\rho_j^{n}}\,\frac{u_{j+1}^{n+1} - u_{j-1}^{n+1}}{2\Delta x} ,$$

$$u_j^{n+1} \geq 0 \qquad 1.4.7$$

The convective terms $u\frac{\partial}{\partial x}$ have been represented in (1.4.5) to (1.4.7) by backward differences. If the velocity is negative, forward differences are to be used in these terms. The equation (1.4.6) is used to advance u from one time step to the next. Then the advanced value of u is used to calculate new values of p, ρ , ε . We have left the equation of state arbitrary. The stability condition is established in Appendix B and is found to be

$$\frac{\Delta t}{\Delta x}\left(|u| + c\right) \leq 1 \qquad 1.4.8$$

which is in agreement with (1.3.7) for the isentropic equations. No significance is attached to the agreement.

1.5 Shock Waves and the Artificial Viscosity

It is difficult to give an exact treatment of shock waves. A useful approximation which permits automatic calculation is due to Richtmyer and Von Neumann (Ref. 7). An artificial viscous pressure is added to the kinetic pressure in equations (1.4.2), (1.4.3). The viscous term is taken to be:

$$q = \begin{cases} l_v^2\,\rho\left(\dfrac{\partial u}{\partial x}\right)^2 & \text{if } \dfrac{\partial u}{\partial x} < 0 \\ 0 & \text{if } \dfrac{\partial u}{\partial x} \geq 0 \end{cases} \qquad 1.5.1$$

The finite difference representation of q is, with $l_v = a \Delta x$

$$q_j^n = \begin{cases} \frac{a^2}{8} \left(\rho_j^n + \rho_{j-1}^n \right) \left(u_{j+1}^n - u_{j-1}^n \right)^2 & \text{if } u_{j+1}^n - u_{j-1}^n \leq 0 \\ 0 & \text{if } u_{j+1}^n - u_{j-1}^n > 0 \end{cases} \qquad 1.5.2$$

Whereas ordinary viscosity would be proportional to the strain rate $\frac{\partial u}{\partial x}$, we have used a quadratic term in $\frac{\partial u}{\partial x}$. The advantage of using a quadratic term in the strain rate is that the shock thickness becomes independent of the shock strength. Richtmyer (Ref. 7) has solved the problem of a plane steady-state shock in a perfect gas with the viscous term. The flow is found to be undisturbed except for a transition zone centered about the "exact" position of the shock and of width:

$$\Delta = \frac{\pi l_v \sqrt{2}}{\sqrt{\gamma + 1}} \qquad 1.5.3$$

Let x_o be the "exact" instantaneous position of the shock wave. Denote properties before and behind the shock wave by subscripts 1 and 2 respectively. Then one has in the transition zone

$$\frac{1}{\rho} = \frac{\frac{1}{\rho_2} + \frac{1}{\rho_1}}{2} + \frac{\frac{1}{\rho_2} - \frac{1}{\rho_1}}{2} \sin \left(\sqrt{\frac{\gamma + 1}{2}} \; \frac{x - x_o}{l_v} \right) \qquad 1.5.4$$

$$u = \frac{u_2 + u_1}{2} + \frac{u_2 - u_1}{2} \sin \left(\sqrt{\frac{\gamma + 1}{2}} \; \frac{x - x_o}{l_v} \right) \qquad 1.5.5$$

$$p + q = \frac{p_1 + p_2}{2} - \frac{p_1 - p_2}{2} \sin \left(\sqrt{\frac{\gamma + 1}{2}} \; \frac{x - x_o}{l_v} \right) \qquad 1.5.6$$

$$q = \frac{p_1 - p_2}{2} \; \frac{\gamma + 1}{2} \; \frac{\left(\cos\left(\sqrt{\frac{\gamma+1}{2}} \; \frac{x - x_o}{l_v}\right)\right)^2}{\frac{\rho_1 + \rho_2}{\rho_1 - \rho_2} + \sin\left(\sqrt{\frac{\gamma+1}{2}} \; \frac{x - x_o}{l_v}\right)} \qquad 1.5.7$$

If shock waves are present at the beginning of the finite difference analysis, (1.5.4) to (1.5.7) may be used to approximate them. The resulting smooth profiles are then suitable for a finite difference technique. The smeared out shock propagates with very nearly the correct velocity (as determined from the Rankine-Hugoniot relations). The calculation proceeds automatically provided we replace p_j^n in equations (1.4.6), (1.4.7) by $p_j^n + q_j^n$ where q_j^n is given by (1.5.2).

The effect of the artificial viscosity on the stability condition is discussed in Appendix C. The maximum permissible time increment is somewhat reduced as the shock strength increases. We found it desirable to use the condition

$$\frac{\Delta t}{\Delta x} \left(|u| \pm c \right) < \frac{1}{2} \qquad 1.5.8$$

1.6 Smoothing Operations

It has been observed by many users of the artificial viscosity that small oscillations or "jitters" often occur during a calculation. These are probably due to insufficient dissipation on the part of the viscous term (Ref. 8). The elimination of small non-physical oscillations has been successfully performed by meteorologists (Ref. 9). We have adopted their techniques.

We wish to define some operator which eliminates small local disturbances from the flow while leaving the rest of the flow pattern unchanged. By a small disturbance is meant one whose wavelength is of the order of $2\Delta x$ where Δx is the grid spacing, and whose amplitude is small. Since shock waves will be present in the flow, such an operator will have to be applied carefully and only in those regions which are known to be free of rapid transitions. We now define a "smoothing element", discuss its properties, and show how more complicated smoothers may be designed. Designating the grid point values of some function $\varphi(x)$ by $\varphi(n\Delta x)$ we write:

$$\bar{\varphi}_n = \varphi(n\Delta x) = \mu\varphi_n + \frac{1}{2}(1-\mu)(\varphi_{n+1} + \varphi_{n-1}) \qquad 1.6.1$$

Equation (1.6.1) defines a three-point smoother. It is useful to write (1.6.1) as:

$$\bar{\varphi}_n = \varphi_n + \frac{\nu}{2}(\varphi_{n-1} + 2\varphi_n + \varphi_{n+1}) \qquad 1.6.2$$

where $\nu = 1 - \mu$ is called the smoothing element index. Let us examine the effect of a smoothing element on a Fourier term. Take:

$$\varphi_n = C + A\cos(k(x_n - \bar{x})) \qquad 1.6.3$$

where k is the wave number and $\bar{x}$ is a phase factor. Substituting (1.6.3) into (1.6.2) one has, upon simplification:

$$\bar{\varphi}_n = C + (1 - \nu(1 - \cos(k\Delta x)))\, A\cos(k(x_n - \bar{x})) \qquad 1.6.4$$

Consequently, the smoothing element changes neither the wave number nor the phase but alters the amplitude by a factor

$$\sigma = 1 - \nu(1 - \cos(k\Delta x)) \qquad 1.6.5$$

If we apply successive smoothing operations with indices ν_0, ν_1, ..., ν_n the final ratio of smoothed to unsmoothed amplitude is easily seen to be

$$\Sigma = \sigma_0 \sigma_1 \ldots \sigma_n = \prod_{m=0}^{n} (1 - \nu_m (1 - \cos(k \Delta x)))$$

One could, in principle, use the above polynomial to curve-fit a smoother to any desired filtering specifications. So far we have been discussing three-point smoothers with real indices. One may equally well define a five-point smoother by:

$$\bar{\varphi}_n = \varphi_n + \frac{\nu}{4} (\varphi_{n-2} + \varphi_{n-1} + \varphi_{n+1} + \varphi_{n+2} - 4\varphi_n)$$

One may verify that a combination of two three-point smoothers whose indices are complex conjugates is equivalent to one five-point smoother with a real index. In our calculations we used a multi-element smoother indicated by Shuman (9), for which the indices were:

$$\begin{aligned} \nu_0 &= 0.45965 \\ \nu_1 &= -0.22227 + i\, 0.64240 \\ \nu_2 &= -0.22227 - i\, 0.64240 \end{aligned} \tag{1.6.6}$$

The multi-element smoother defined by (1.6.6) was applied periodically to those regions of the flow known to be free of shock waves. The resulting operator proved very effective in eliminating short wave disturbances while leaving the rest of the field untouched.

1.7 Details of the Finite Difference Schemes

The finite difference representation of the isentropic equations (1.4.5), (1.3.6) was given in Section 1.3. It is the purpose of this section to indicate the details of its use. The non-isentropic equations (1.4.5), (1.4.6), (1.4.7) are to be handled analogously.

Consider Fig. 1.4.

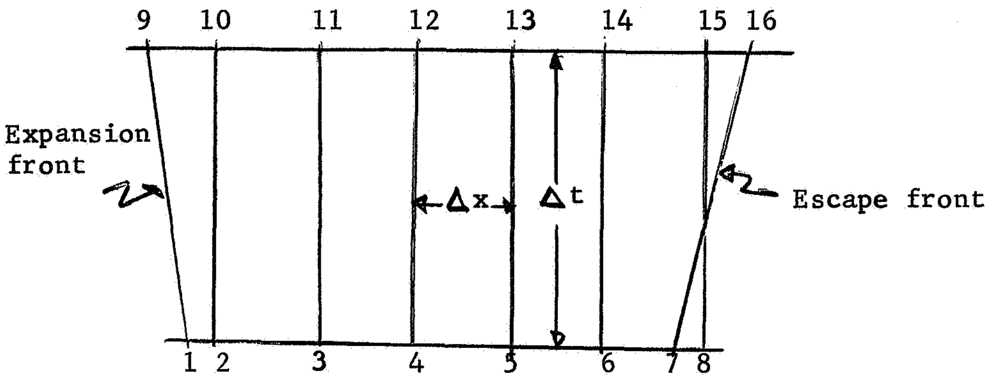

Detail of Finite Difference Grid

Fig. 1.4

Equations (1.3.5), (1.3.6) involve centered spatial differences. Evidently values at the grid points 11, 12, and 13 may be written down by direct application of (1.3.5), (1.3.6). However, one must be more careful at 10, 14, and 15. An attempt to calculate centered differences at 2, say, will take us outside the boundaries. Therefore, at point 2 we use as an approximation to $\frac{\partial u}{\partial x}$:

$$\frac{\partial u}{\partial x} \simeq \frac{1}{2}\left(\frac{u(2)-u(1)}{\beta} + \frac{u(3)-u(2)}{\Delta x}\right) \qquad 1.7.1$$

where β is the distance between 1 and 2. If $\beta \rightarrow \Delta x$ then (1.7.1) tends to the usual centered form. Substitution of (1.7.1) into (1.3.5), (1.3.6) permits us to calculate the new values of u and c at point 10. A similar procedure is followed at point 14. Then the value at 15 may be obtained by linear interpolation between 14 and 16 on the boundary where values are presumed known.

One may note that the first term on the right hand side of (1.7.1) is a suitable representation for a backward difference at point 2. Forward differences may be defined analogously. With this observation in mind one may extend the above techniques to the non-isentropic difference equations (1.4.5) to (1.4.7).

1.8 Treatment of the Pellet and Bumper Rarefactions

The initial discontinuity which occurs at the downstream free surface of the bumper at the moment when $\overleftarrow{\mathcal{R}}_B$ is generated is easily treated via equations (1.2.3), (1.2.4). In terms of the notation of Section 1.2 we write

$$\delta = t - t_o \qquad 1.8.1$$

and choose δ so that the width of the rarefaction fan at time $t_o + \delta$ corresponds to four or five grid spaces. The width of the fan is, of course, determined from equations (1.2.1), (1.2.2). In this way the initial discontinuity at time t_o is removed and the only change in the rest of the flow is that the uniformly moving boundaries are advanced by the appropriate amount.

The initialization of $\overrightarrow{\mathcal{R}}_p$, however, cannot be handled quite so neatly. Two possibilities exist:

(i) When shock decay occurs, and the artificial viscosity is used to produce a shock of finite thickness whose leading edge reaches the upstream free surface of the pellet.

(ii) When no shock decay occurs, no artificial viscosity is used, and a shock of zero thickness reaches the upstream free surface of the pellet.

In case (i) we make use of the finite distribution of the shock wave.

We arbitrarily determine the escape time as that instant when the leading edge of $\overleftarrow{S}_p$ reaches the upstream pellet edge. At that time escape conditions are determined from the flow values at the point of maximum pressure and values at this point are joined linearly with the predicted escape values at the pellet boundary. In this way no time step is involved and the rest of the field is left unchanged. A small error is introduced in that a small quantity of pellet mass is lost. This error is, however, comparable with the uncertainty in the time of arrival of the shock wave at the upstream pellet boundary.

If we write x_o as the position of the pellet boundary at the chosen escape time and x_1 for the position of the pellet maximum, our escape boundary conditions are:

$$\begin{aligned} \rho(x_o) &= 0 \\ p(x_o) &= 0 \\ u(x_o) &= u(x_1) - \frac{2}{\gamma_p - 1}\sqrt{\gamma_p \frac{p(x_1)}{\rho(x_1)}} \end{aligned} \qquad 1.8.2$$

Although no tests were made in which case (ii) occurred, as the primary object of the program was essentially to study period III and the subsequent shock decay, provision was made to allow such a possibility. The free surface was handled in the fashion described in Section 1.2 for the bumper free surface except that we used values of the flow variables appropriate to the pellet material. This is permissible as long as the expansion front of the rarefaction $\overrightarrow{\mathcal{R}}_p$, generated at the pellet free surface, is not permitted to enter the regime of $\overleftarrow{\mathcal{R}}_B$ in the process of initialization.

One must then adjust the rest of the field to the new time $t_o + \delta$. Equations (1.2.3), (1.2.4) were not used in order to avoid generating instabilities. Instead it was noted that the various profiles retained geometric similarity during the prior computation. Therefore, it was assumed that the decay profiles in the rarefaction zone would retain their shape during the small time interval δ .

Writing x_o and x_1 for the positions of the expansion and escape fronts associated with $\overleftarrow{\mathcal{R}}_B$ we have:

$$\begin{aligned} x_o &\longrightarrow x_o^{1} = x_o + (u_o - c_o)\delta \\ x_1 &\longrightarrow x_1^{1} = x_1 + u_1\delta \end{aligned} \qquad 1.8.3$$

where

$u_o = u(x_o)$

$c_o = c(x_o)$

$u_1 = u(x_1)$ = escape velocity.

The new profiles are taken to be

$$\begin{aligned} c(x,t_o + \delta) &= c\left(\frac{x_1 - x_o}{x_1^{1} - x_o^{1}}(x - x_o^{1}) + x_o,\ t_o\right) \\ u(x,t_o + \delta) &= u\left(\frac{x_1 - x_o}{x_1^{1} - x_o^{1}}(x - x_o^{1}) + x_o,\ t_o\right) \end{aligned} \qquad 1.8.4$$

where t_o was the time at which $\overrightarrow{\mathcal{R}}_p$ was generated.

In both cases (i) and (ii) it is assumed that the escape front velocity remains constant. In fact this is a consequence of the uniformity of the material bounded by the free surface assumed in Section 1.2 and is not true in general. However, it is felt to be justified *a posteriori* by the subsequent calculation in which the velocity field was seen to increase monotonically from the upstream pellet escape value.

1.9 Treatment of the Contact Front

In general a contact discontinuity must be handled by interior fitting procedures which are accurate to the second order in the grid spacing Δx. (Ref. 7).

If, however, a functional representation of the entropy is available, it may be possible to write the transition properties directly. In this report only a perfect gas is considered. If we note that particles on either side of the contact front retain their shocked entropy values throughout the entire subsequent analysis, we may write:

$$\frac{p_p}{\rho_p^{\gamma_p}} = \left(\frac{p_p}{\rho_p^{\gamma_p}}\right)_o \qquad 1.9.1$$

$$\frac{p_B}{\rho_B^{\gamma_B}} = \left(\frac{p_B}{\rho_B^{\gamma_B}}\right)_o \qquad 1.9.2$$

where the right hand sides are evaluated in the initial shocked state and the equalities hold at the contact front for all subsequent times.

Since we are dealing with a contact surface we may write:

$$\begin{aligned} u_p &= u_B \\ p_p &= p_B \end{aligned} \qquad 1.9.3$$

These are the transition relations for pressure and velocity across the contact surface.

Using the second equation in 1.9.3 and dividing 1.9.1 by 1.9.2 we arrive at

$$\left(\frac{\rho_B}{\rho_{B_o}}\right)^{\gamma_B} = \left(\frac{\rho_p}{\rho_{p_o}}\right)^{\gamma_p} \qquad 1.9.4$$

which is valid for all times subsequent to the initial instant of impact.

Since $\rho_{B_o} = 1$ in our non-dimensional scheme we have the transition formulae:

$$\rho_B = \left(\frac{\rho_P}{\rho_{P_o}/\rho_{B_o}}\right)^{\gamma_P/\gamma_B} \qquad 1.9.5$$

and

$$\rho_P = \left(\frac{\rho_{P_o}}{\rho_{B_o}}\right)\rho_B^{\;\gamma_B/\gamma_P}$$

As the velocity of the contact front, C, relative to the flow is zero, we may advance its position each time step as follows:

Let f be the position of C, $i - 1 \leq f \leq i$

$$f(t + \Delta t) = f(t) + \frac{\Delta t}{\Delta x}\left(u_{i-1}\,(i - f) + u_i\,(f - i + 1)\right)$$

where $u_{i-1} = u((i - 1)\Delta x, t)$

During computation with the non-isentropic equations, equations (1.9.5) were used to convert directly terms appearing in differences taken across the contact front.

i.e. With $i - 1 \leq f \leq i$ we write a backward difference as:

$$\left.\frac{\partial \rho}{\partial x}\right|_i \simeq \frac{\rho_i - \left(\dfrac{\rho_{i-1}}{\rho_{P_o}/\rho_{B_o}}\right)^{\frac{\gamma_P}{\gamma_B}}}{\Delta x} \qquad 1.9.6$$

Similarly a forward difference at grid point i - 1 is written

$$\left.\frac{\partial \rho}{\partial x}\right|_{i-1} \simeq \frac{\frac{\rho_{p_o}}{\rho_{B_o}}\,\rho_i^{\frac{\gamma_B}{\gamma_p}} - \rho_{i-1}}{\Delta x} \qquad 1.9.7$$

Centered differences may be constructed by averaging the expressions in (1.9.6), (1.9.7) with the usual forward difference at i or the backward difference at i-1 (such terms are unaffected by the contact front as differences are not taken across it).

Of course, the internal energy, $\mathcal{E}$, must be similarly converted by substitution of an adjusted density value in the functional equation whenever necessary.

In the isentropic case we require a conversion rule for c, the isentropic sound speed.

We have, in virtue of the continuity of pressure:

$$\frac{c_p}{c_B} = \sqrt{\frac{\gamma_p}{\gamma_B}\,\frac{\rho_B}{\rho_p}}$$

across the contact front. Using the second equation in (1.9.5), we have:

$$c_p = c_B \sqrt{\frac{\gamma_p}{\gamma_B}\,\frac{\rho_{B_o}}{\rho_{p_o}}\,\rho_B^{\frac{\gamma_p - \gamma_B}{\gamma_p}}} \qquad 1.9.8$$

Since $\frac{p}{\rho_B^{\gamma_B}} = \lambda$, a constant, we may write

$$\rho_B = \left(\frac{c^2}{\gamma_B \lambda} \right)^{\frac{1}{\gamma_B - 1}}$$

We now substitute this into the equation 1.9.8 to eliminate ρ_B. This gives us:

$$c_p = c_B \quad 1 + \frac{\gamma_p - \gamma_B}{\gamma_p(\gamma_B - 1)} \left(\frac{\gamma_p}{\gamma_B} \frac{\rho_{B_o}}{\rho_{p_o}} (\lambda \gamma_B)^{\frac{p - B}{p(1- B)}} \right)^{\frac{1}{2}}$$

So we may write

$$c_p = A\, c_B^{\ B} \tag{1.9.9}$$

where

$$A = \left(\frac{\rho_{B_o}}{\rho_{p_o}} \frac{\gamma_p}{\gamma_B} (\lambda \gamma_B)^{\frac{\gamma_p - \gamma_B}{\gamma_p(1 - \gamma_B)}} \right)^{\frac{1}{2}}$$

$$B = \frac{\gamma_B (\gamma_p - 1)}{\gamma_p (\gamma_B - 1)}$$

Then 1.9.9 and its inverse are used to represent centered differences in the same way as above.

This technique assumes that the profiles on either side of the contact front are geometrically similar, and inspection of a sample calculation supports this assumption. Of course, the accuracy is proportional to the fineness of the spatial mesh.

We chose the convention that when the contact front coincided with a grid point, that grid point assumed pellet values.

1.10 Interaction of the Gas Cloud With a Secondary Surface

If a secondary surface is present, the leading edge of the cloud will interact with it after some initial period of expansion and a reflected shock wave will be produced. Let the subscripts 0 and 1 denote properties before and behind the wave respectively and let the shock velocity in a laboratory frame of reference be D. Then

$$(1 - \mu^2)(D - u_0)^2 - (u_1 - u_0)(D - u_0) - (1 - \mu^2)\, c_0^{\,2} = 0 \qquad 1.10.1$$

where $\mu^2 = \dfrac{\gamma - 1}{\gamma + 1}$. Equation (1.10.1) may be deduced from the jump conditions across a shock.

$$D = u_0 + \frac{(u_1 - u_0) \pm \sqrt{(u_1 - u_0)^2 + (1 - \mu^2)\, c_0^{\,2}}}{2(1 - \mu^2)} \qquad 1.10.2$$

For a travelling wave one chooses the positive sign. ρ_1 and p_1 may be obtained from the mass and momentum relations respectively:

$$\rho_1 = \rho_0 \frac{(u_0 - D)}{(u_1 - D)} \qquad 1.10.3$$

$$p_1 = p_0 + \rho_0 (u_0 - D)^2 - \rho_1 (u_1 - D)^2$$

We now apply the stagnation requirement at the stationary plate:

$$u_1 = 0$$

We now have enough information to determine ρ_1 and p_1 so that the shock is completely specified. Consequently we may approximate the initial reflected shock according to equations (1.5.4) to (1.5.6). The finite difference solution can then be continued automatically.

It is useful, however, to make a qualitative study of the reflected shock. If we note that $c_0 \simeq 0$ near the escape front at the moment of interaction, we may write equation (1.10.2) as

$$D \simeq u_0 + \frac{-u_0 + (-u_0)}{2(1 - \mu^2)} \qquad 1.10.4$$

where we have written $u_1 = 0$.

Consequently

$$D \simeq u_0 \left(1 - \frac{1}{1 - \mu^2}\right) = \frac{2u_0}{\gamma + 1} \qquad 1.10.5$$

Whence from 1.10.3 we have

$$\rho_1 = \rho_0 \frac{\gamma + 1}{\gamma - 1} \qquad 1.10.6$$

$$p_1 = \rho_0 u_0^2 \frac{(\gamma + 1)}{2} \qquad 1.10.7$$

(ignoring the initial pressure p_0).

Equation (1.10.6) is the natural consequence of the strong shock assumption

$$D >> c_0$$

However (1.10.7) is of more immediate interest. In the undisturbed flow the total pressure consists mainly of the dynamic term $\frac{\rho u^2}{2}$. If we now observe that for long term expansion c_0^2 is negligible in equation (1.10.2) throughout the flow, and if we suppose $u_1 \equiv 0$ behind the shock wave at all times, then (1.10.5) to (1.10.7) remain valid throughout the flow. While ignoring the possibility of back flow, these assumptions are adequate for a qualitative analysis.

It then follows from (1.10.7) that the pressure behind the reflected shock is approximately (γ + 1) times the total pressure at that point in the undisturbed flow. Now if the velocity is constant behind the shock wave, we expect from the momentum equation

$$\frac{\partial u}{\partial t} + u\frac{\partial u}{\partial x} + \frac{1}{\rho}\frac{\partial p}{\partial x} = 0$$

that $\frac{\partial p}{\partial x} = 0$. In other words, the pressure behind the shock wave is a good indication of the pressure at the secondary surface. Consequently, we expect that the pressure at the secondary plate will be of the order of (γ + 1) times the maximum total pressure observed at the same point in the undisturbed flow. This is in line with the experimental observations.

For the initialization of the wave we make use of the finite distribution of the transition zone determined by the coefficient of artificial viscosity. The trailing edge of the wave is identified with the plate position so that the position of the leading edge is determined from equation (1.5.3). The quantities u_o, p_o, ρ_o are evaluated at the leading edge whence ρ_1, p_1 are given by equations (1.10.6) and (1.10.7). The distributions in the transition zone are determined from equations (1.5.4) to (1.5.6). At later times the boundary value for u is known, u = 0 and boundary values for ρ , p are obtained from an extrapolation of the two adjacent grid points.

CHAPTER TWO

2.1 Results and Discussion

A successful calculation was made for a like material impact with a pellet to bumper length ratio of 8 and $\gamma_p = \gamma_B = 3$. The results of this calculation are depicted graphically in Figs. 2.1 to 2.13. In Figs. 2.1 to 2.4, the profiles of the fluid properties during the destruction of the pellet are shown; Figs. 2.5 to 2.7 show the profiles during the period of total expansion; and Figs. 2.8 to 2.10 show the profiles during the interaction of the flow with a secondary surface located 100 bumper thicknesses downstream from the point of impact. Fig. 2.11 makes a comparison of the total pressure at the secondary surface with the total pressure at the same point in undisturbed flow. Fig. 2.12 shows the peak pressure behind the pellet shock, $\overleftarrow{S}_p$, as a function of time, while Fig. 2.13 shows the position of $\overleftarrow{S}_p$ as a function of time. All data is presented in the non-dimensional form discussed in Section 1.1. Successful calculations were also performed with a pellet to bumper ratio of 9 for like material impacts with γ taken successively to be 1.4, 3 and 7. A further test was made with $\gamma_p = \gamma_B = 3$ and $l_p = 9$, but with a pellet to bumper density of 2, in order to check the contact surface technique discussed in Section 1.9. As the purpose of these tests was merely to examine the range of applicability of the computer program, the results are not presented in this report.

A storage array of 250 grid points was considered adequate for the calculation presented here. The profiles of the fluid parameters at the instant when $\overrightarrow{S}_B$ reached the downstream free surface of the bumper were calculated from equations (1.1.10) to (1.1.13) and were represented by distributions over 100 grid points located symmetrically in the field of 250. The bumper rarefaction was initialized with the help of equations (1.2.3) and (1.2.4) and the calculation of the profiles at subsequent time steps proceeded using the isentropic equations (1.3.5) and (1.3.6). The grid ratio was taken to be $\frac{\Delta x}{\Delta t} = 5$ as recommended in Ref. 3. As may be seen from Figs. 2.1 to 2.3, the pressure and density profiles decrease monotonically in the rarefaction zone while the velocity increases monotonically.

Once the rarefaction $\overleftarrow{\mathcal{R}}_B$ had approached the pellet shock $\overleftarrow{S}_p$, $\overleftarrow{S}_p$ was represented by the "shock layer" profiles of equations (1.5.4) etc. The coefficient of artificial viscosity was taken to be $a = 2.5$. Then the calculation of the subsequent flow proceeded using the finite difference scheme (1.4.5) etc. with the viscous term. Smoothing was performed every 25 time steps according to equation (1.6.6). As may be seen from Fig. 2.12, the pressure behind $\overleftarrow{S}_p$ is considerably diminished by the bumper rarefaction. In this ideal model, no vaporization energy was considered. Consequently the program contained no automatic procedure for the determination of some critical shocked pressure that would just correspond to pellet vaporization. It would, however, be possible to make such a decision and to study the dynamics of pellet destruction. The validity of the one-dimensional approach is, of course, restricted to the early time interaction, before radial attenuation becomes important. But the pellet destruction takes place in just that period, so that the relatively simple one-dimensional model may be employed with a reasonable measure of confidence.

Although it was understood that this model would predict profiles in gross error for the long term expansion, it was considered desirable to determine the stability of the computer code in this case and to attempt a preliminary analysis of the secondary plate interaction. When $\overleftarrow{S}_p$ reached the upstream pellet edge, the release wave $\overrightarrow{\mathcal{R}}_p$ was initialized according to equations (1.8.2), and the solution continued up to time t = 10.

In order to continue the solution out to large distances, it was necessary at this point to reduce the profiles to a spread of 25 to 40 grid intervals. This had the effect of decreasing the computation time considerably. It was expected that a loss of accuracy would be incurred in this way due to the truncation error in the finite difference approximations. In fact, increasing losses in mass and energy were observed throughout this part of the calculation. Figs. 2.5, 2.6, 2.7 represent the fluid profiles at times 50, 70, 100 and 150 respectively. We have not presented the negligible static pressure.

It may be observed from Figs. 2.4 and 2.7 that the initial double peak in total pressure gradually tends to a single peak located toward the front of the cloud. The first of these two peaks located towards the front of the cloud is essentially a dynamic contribution $\frac{\rho u^2}{2}$, whereas the other is due to a local static pressure maximum behind the pellet shock. During the phase of total expansion, the static pressure tends uniformly to zero and only the first peak remains. The velocity curve tends to become linear by time t = 30 except for a small flattening effect near the bumper escape front. This flattening is probably anomalous and without physical reality. Near the escape front the pressure and density tend to such small values that computational inaccuracies are generated by the finite digital representation of the computer. Several attempts were made to counteract the losses in mass and energy which were discovered. Sample calculations with a finer mesh indicated that they were indeed due to the coarse mesh chosen for computational rapidity.

However, an examination of Figs. 2.5 to 2.7 reveal that the flow becomes self-similar once the pressure has diminished to the point of negligibility. This is to be expected and is supported by a similarity analysis of the problem (Ref. 3). One could therefore compute the profiles at time 200 directly from those at time 30 via the observed geometrical similarity.

The loss in mass by the time the gas had reached a point 100 bumper thicknesses downstream was roughly 25%. However, since there was not likely to be experimental confirmation of the profiles predicted so far out of the range of validity of the one-dimensional assumption, it did not seem economically worthwhile to perform the calculation with a finer grid.

When the leading edge of the expansion cloud was 100 bumper thicknesses downstream from the point of impact, secondary plate boundary conditions were established via equations 1.10.6, 1.10.7. The wave was initialized to a spread somewhat longer than that determined by a viscosity coefficient of 2.5. This was not always necessary, as calculations with data at different times and with different impact data have indicated. However, for this particular case insufficient shock spread caused the wave to collapse back into the plate. Presumably one should supply more information about the physics of the interaction in order to remove the ambiguity caused by the absence of known boundary values for the density and pressure.

As can be seen from Fig. 2.10, the pressure at the wall increases to a maximum quickly since the initial mass distribution peaks towards the front of the cloud. The pressures behind the reflected shock are roughly constant.

Fig. 2.9 shows that backflow is predicted in agreement with experimental observations. From Fig. 2.11 it would appear that the reflected and free stream pressure pulses are roughly similar in shape. The reflected pulse has a maximum approximately four times the free stream pulse. Since γ was taken to be 3, this is in surprisingly good agreement with the naive analysis of Section 1.10.

Secondary plate calculations were performed for a plate 5 bumper thicknesses downstream from the point of impact as a preliminary to the calculation shown here. As such a calculation is well within the bounds of applicability of a one-dimensional model, we will mention the most important features of the results. At such an early stage in the expansion, the pellet shock was still in progress and cloud pressures were typically at the impact level. The assumption of a perfectly reflecting wall led to enormous reflected pressures. Consequently, the presence of any internal lining between a bumper and the hull could produce disastrous results even under the assumption that the lining does not vaporize. If the lining itself should vaporize, one may expect violent damage to the neighboring hull due to the very high pressures associated with the impacted lining.

In Fig. 2.12 the pressure behind the pellet shock has been plotted as a function of time. As can be seen, the dependence is roughly linear. Due to the decrease in pressure, $\overleftarrow{S}_p$ tends to be accelerated downstream. Taking the pellet shock position to be located in the center of the finite shock layer, one may plot it versus time. This is done in Fig. 2.13.

Figs. 2.12 and 2.13 give a fairly reliable indication of the impact dynamics. The accuracy involved depends on the fineness of the space grid, since the finite distribution of the shock wave in the von Neumann theory causes earlier interference with the bumper rarefaction than a calculation based on an ideal discontinuous shock.

2.2 Concluding Remarks

Although the basic motivation for this research was to understand the dynamics of the hypervelocity impact, we were largely concerned with computational difficulties. Consequently, while we have developed a useful model for the early stages of the interaction, the results presented here represent for the most part mathematical rather than physical progress.

By writing in new hydrodynamic code we wanted to solve two problems which have caused difficulties, namely the long term stability and the "jitters" associated with the artificial viscosity. The program has been largely successful in both respects. The program was computationally stable during all phases of the expansion. The losses in mass due to truncation errors can be avoided by the use of a finer mesh during the later part of the calculation. This need not be overly expensive as the flow quickly becomes self-similar once the pellet is entirely vaporized. One, therefore, need only use the finite difference scheme during the early stages of total expansion. The late time profiles may be obtained by a similarity transformation.

The technique of using a smoother in conjunction with an artificial viscosity does not seem to have occurred to fluid dynamicists at large. The method is, of course, quite familiar in meteorology where it is used to delete unphysical oscillations of short wavelength. We used it as an additional mode of dissipation. Because the "jitters" usually appear first in the density profile, the artificial viscosity is not brought into play immediately (see equation 1.5.2). Consequently additional dissipation is necessary. (One may define dissipative terms dependent on the density gradients but their properties in the transition zone make them difficult to deal with.)

The program as developed is well suited to the study of the meteoroid-bumper interaction. During the period of interaction, the one-dimensional approximation has reasonable validity. It would be useful to use a real gas equation of state and to consider the effects of vaporization energy. In this way one would be able to predict automatically the destructive properties of various pellet-bumper systems in the intermediate velocity range where vaporization energy is not negligible. This is especially desirable as the experimental velocities belong to such an intermediate range.

The secondary plate calculation produced results in rather good agreement with a very simplified analysis. The maximum reflected pressure was found to be roughly (γ + 1) times the maximum free stream pressure. Experimentally, the two maxima appear to be roughly the same. However, radial relaxation of the reflected shock is likely to be important in the two-dimensional case.

The assumption of a perfectly reflecting wall led to enormous reflected pressures when the bumper and wall were very close to each other. The pressures were of the order of the shock pressures. Therefore, the presence of an internal filler between a bumper and the spacecraft hull could produce disastrous results if the shock wave is able to propagate through the filler to the hull or if the filler is sufficiently shocked to vaporize, producing gas under very high pressures in a confined volume, as these pressures could produce very large ruptures in the adjacent hull. The differences in impact pressures between lower velocity experimental impacts and the higher velocity meteoroid impacts may produce very different results with filler materials. Even at currently available laboratory velocities, a catastrophic rupture due to filler vaporization may be observed.

Friend et al. (Ref. 10) describe impacts onto a system consisting of two parallel sheets filled with polyurethane. The expanding vapor cloud from the outer sheet induced pyrolysis of the filler, producing a high pressure gas in a confined volume. The resulting rupture was far greater than that observed in the unfilled system.

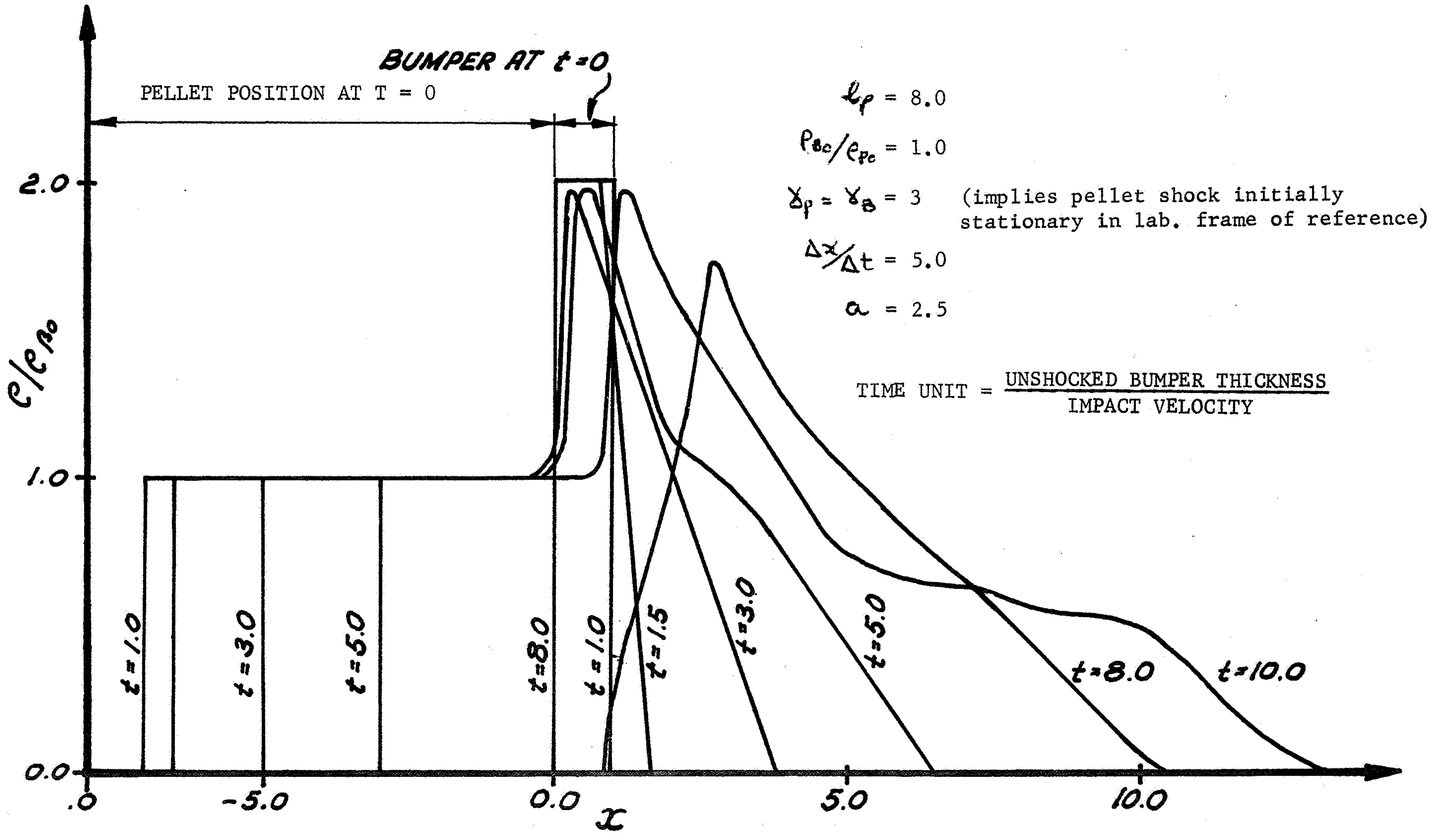

Fig. 2.1 Distributions of Non-Dimensional Density vs. Axial Distance in Units of Initial Bumper Thickness

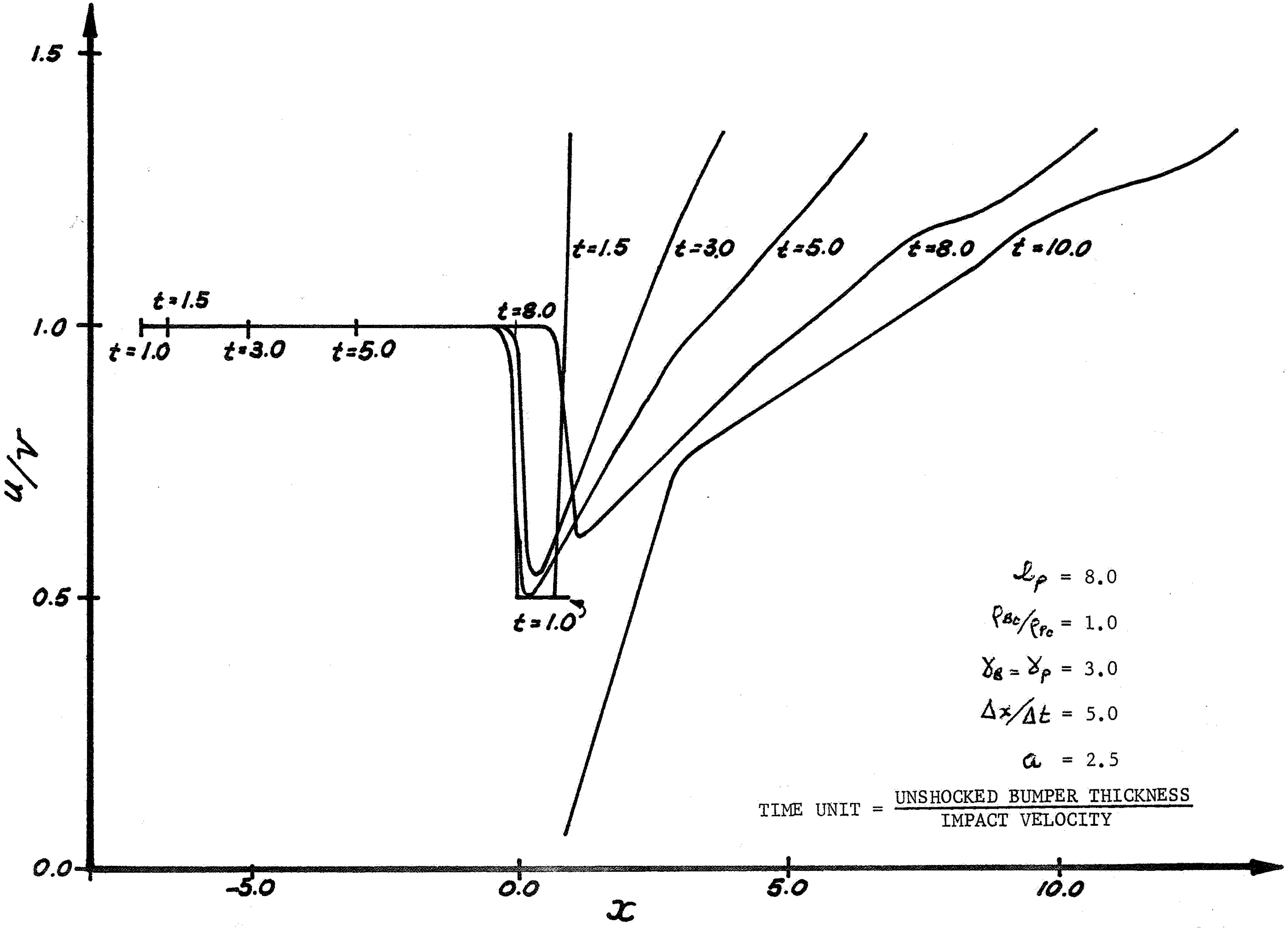

Fig. 2.2. Non-Dimensional Particle Velocity vs. Axial Distance in Units of Initial Bumper Thickness

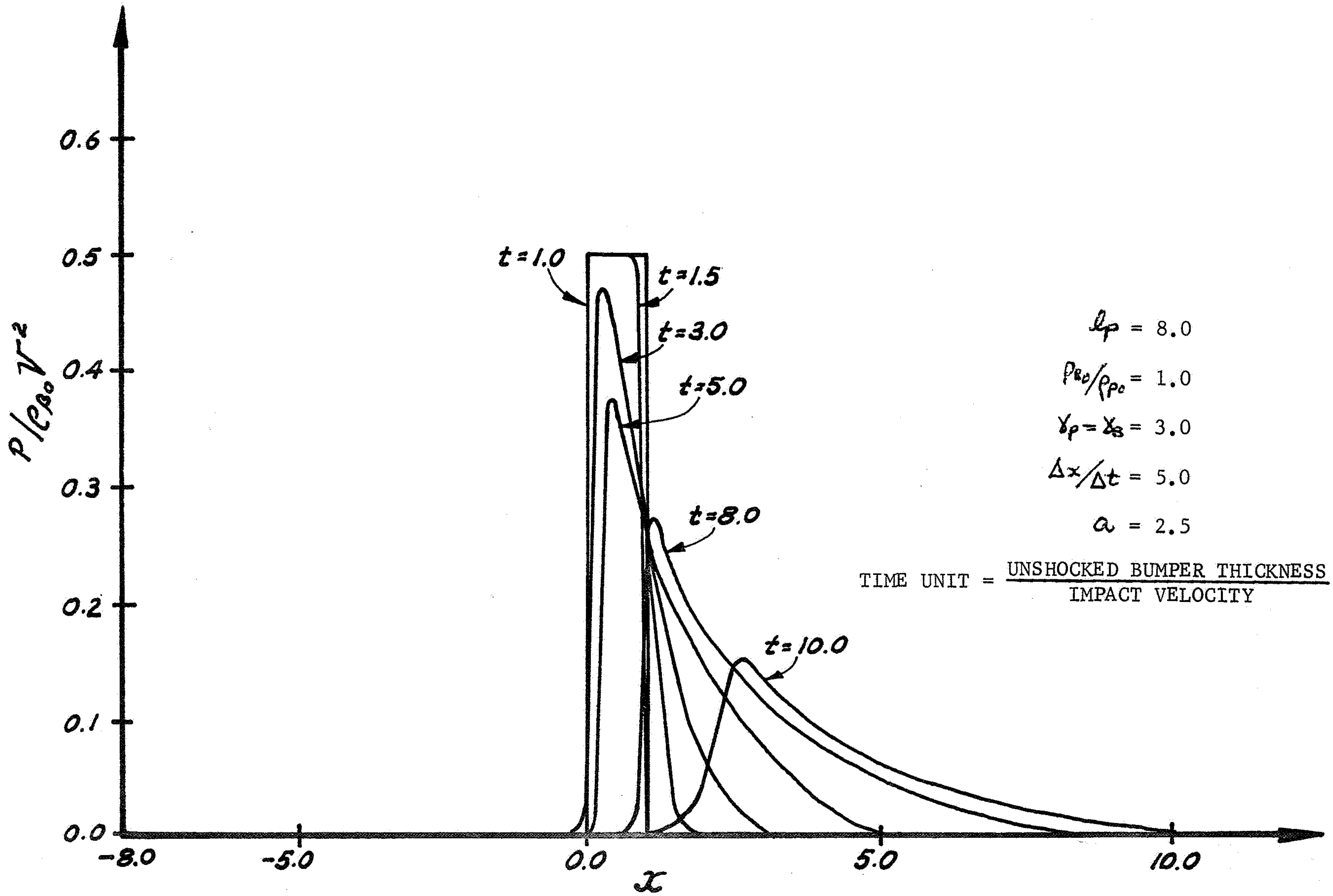

Fig. 2.3 Non-Dimensional Pressure vs. Axial Distance in Units of Initial Bumper Thickness

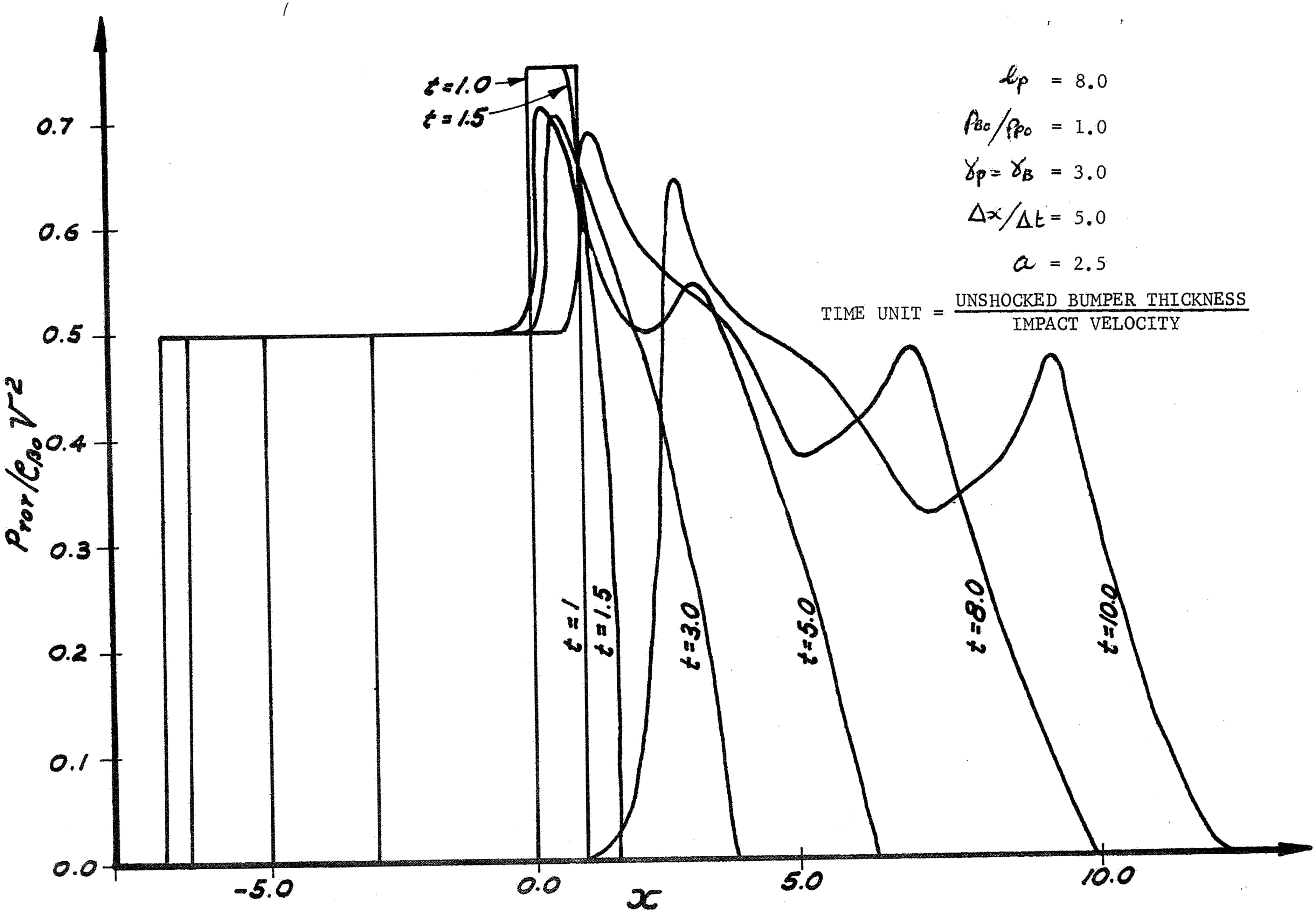

Fig. 2.4 Profiles of Total Non-Dimensional Pressure vs. Axial Distance in Units of Initial Bumper Thickness

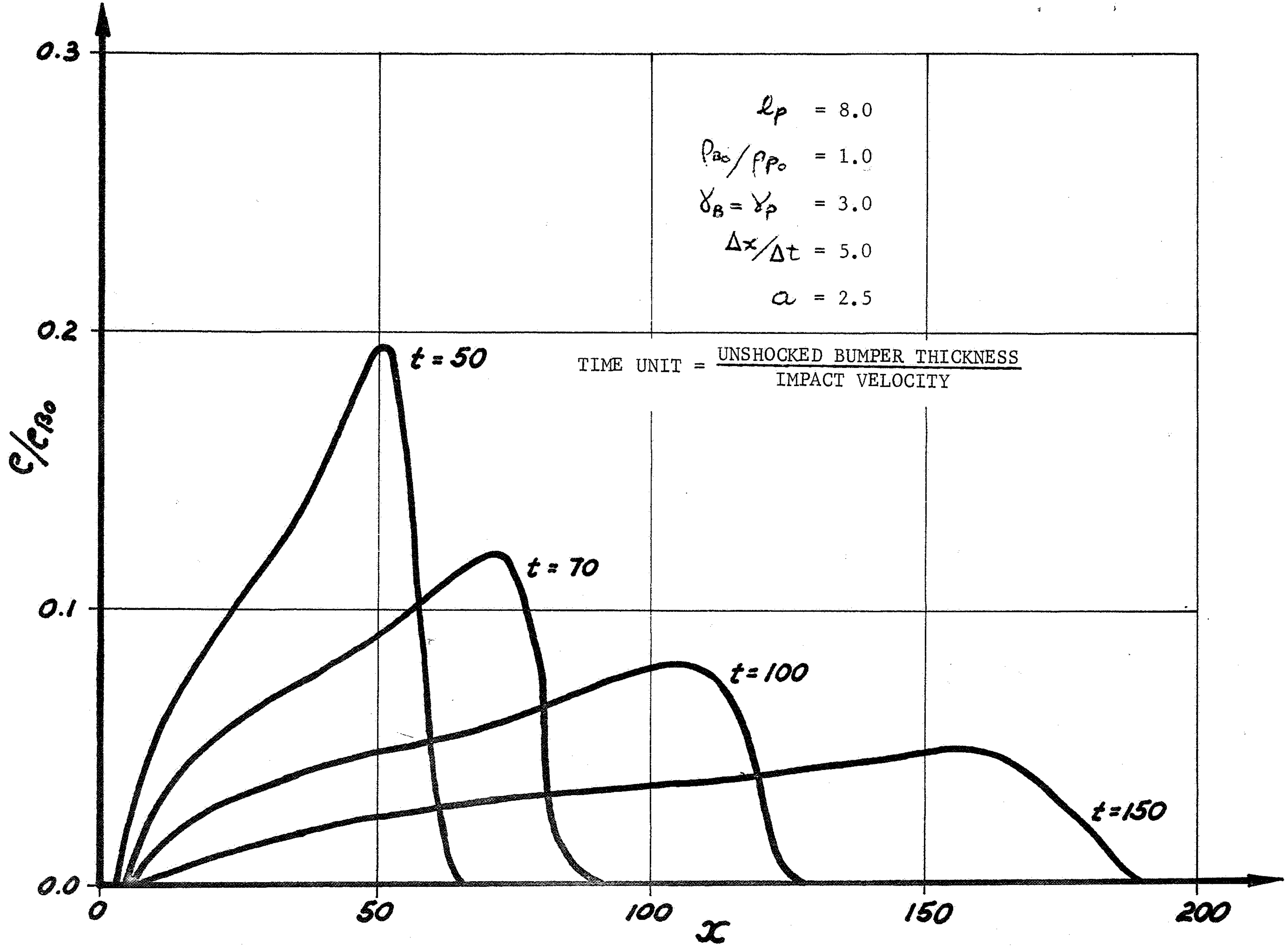

Fig. 2.5 Profiles of Non-Dimensional Density vs. Axial Distance in Units of Initial Bumper Thickness during Expansion Process

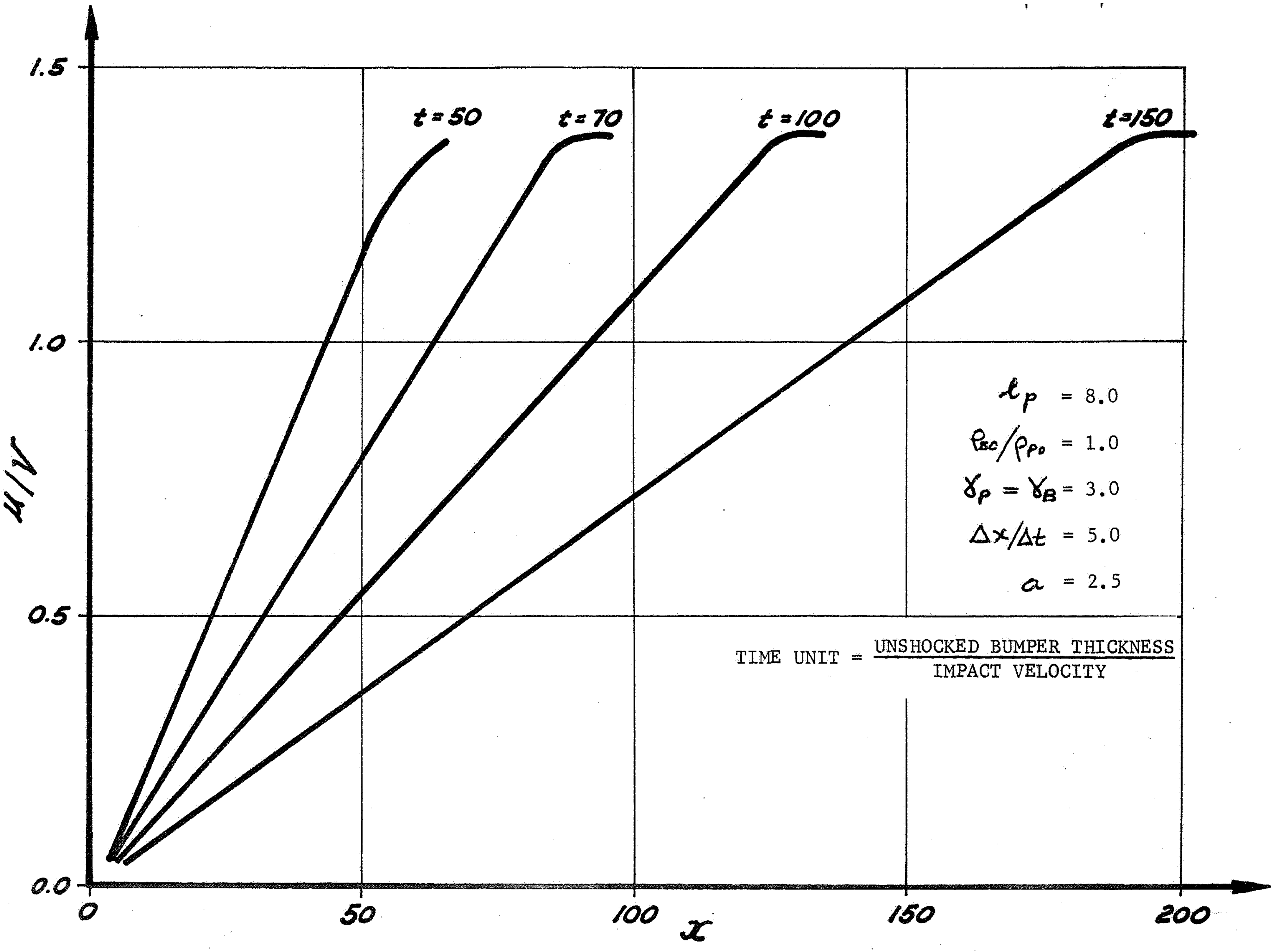

Fig. 2.6 Profiles of Non-Dimensional Particle Velocity vs. Axial Distance in Units of Initial Bumper Thickness during Expansion Process

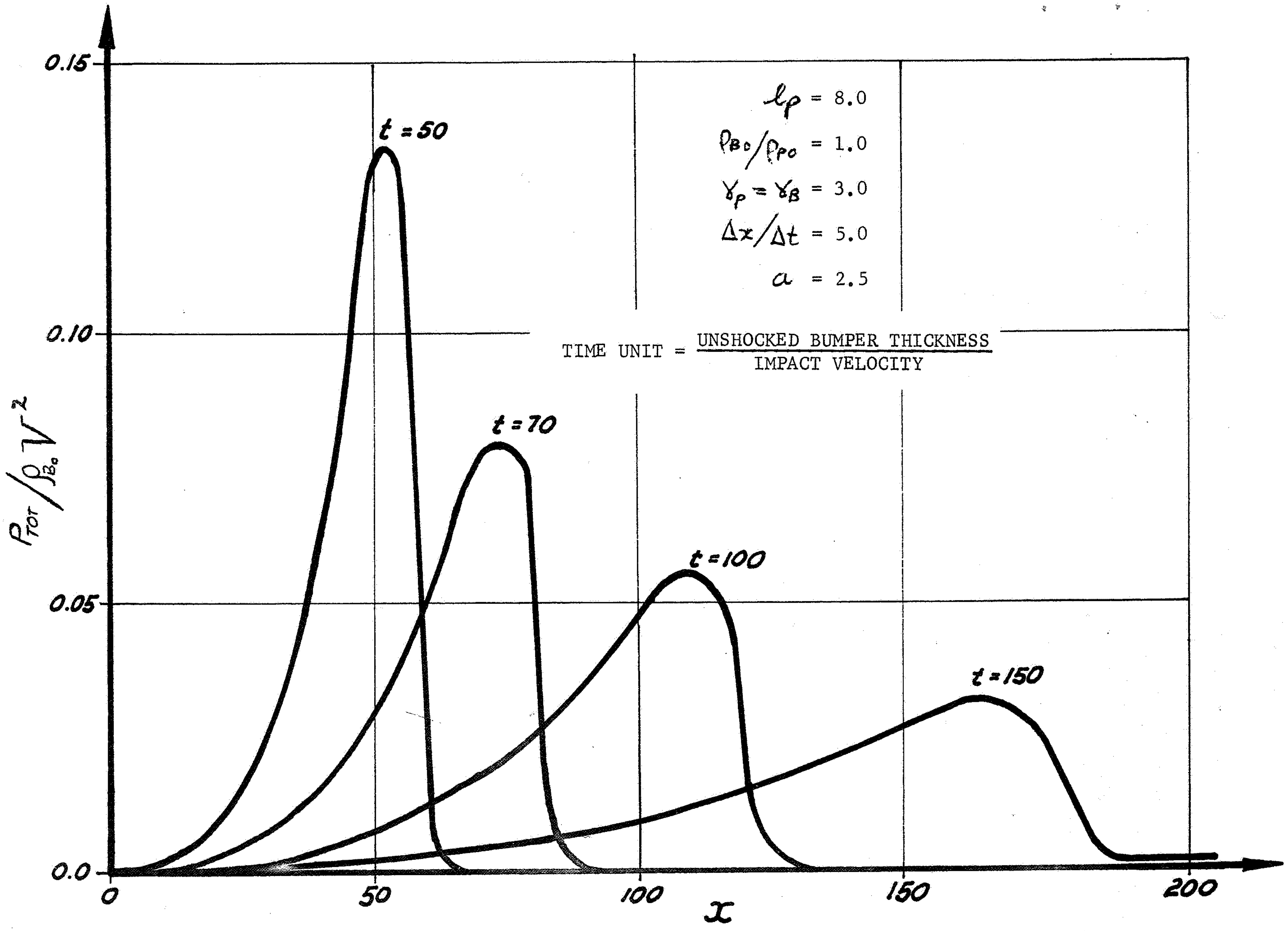

Fig. 2.7 Profiles of Non-Dimensional Total Pressure vs. Axial Distance in Units of Initial Bumper Thickness

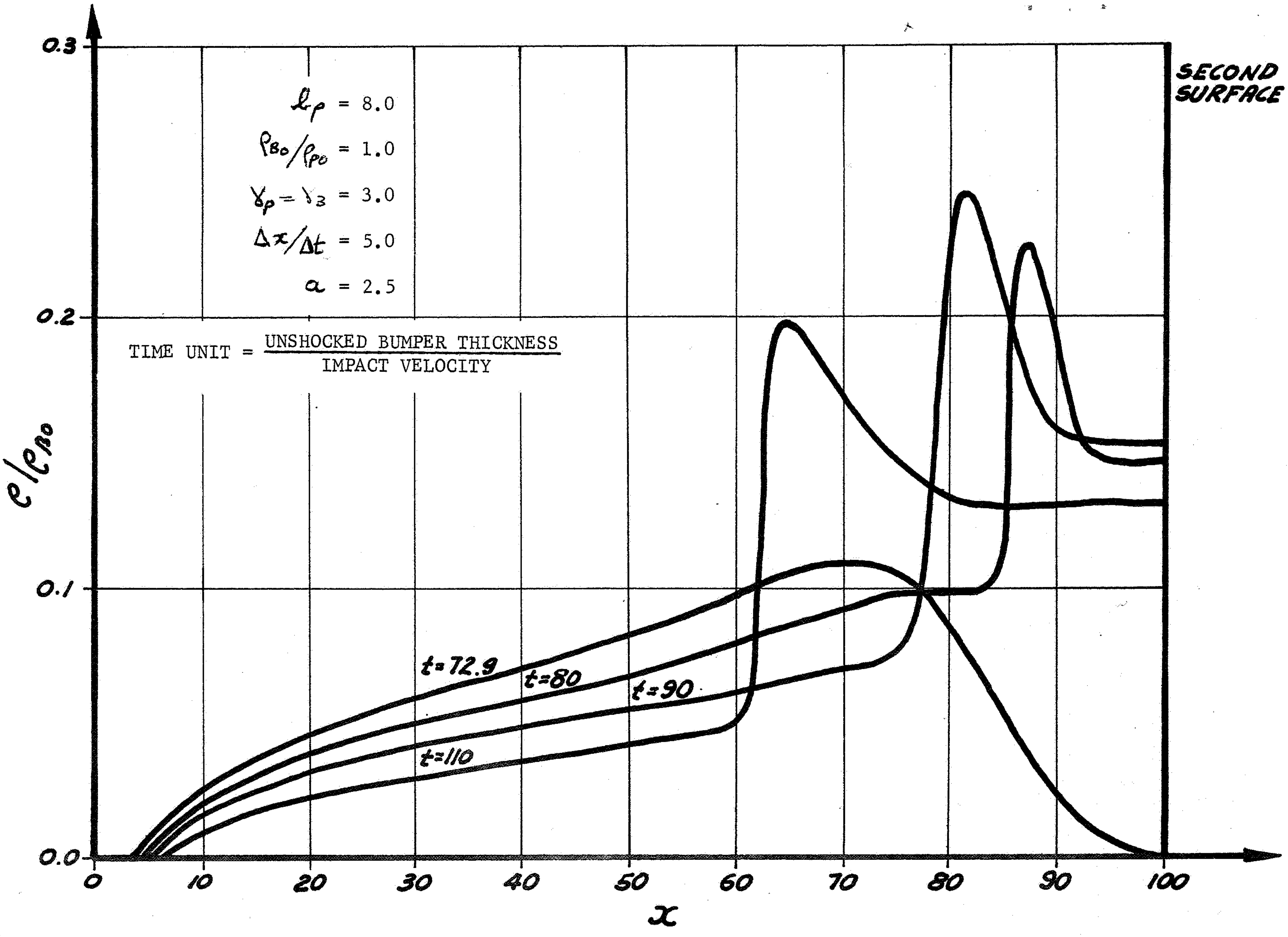

Fig. 2.8 Non-Dimensional Density Profiles for Interaction of the Gas Cloud with a Secondary Surface 100 Bumper Thicknesses Downstream

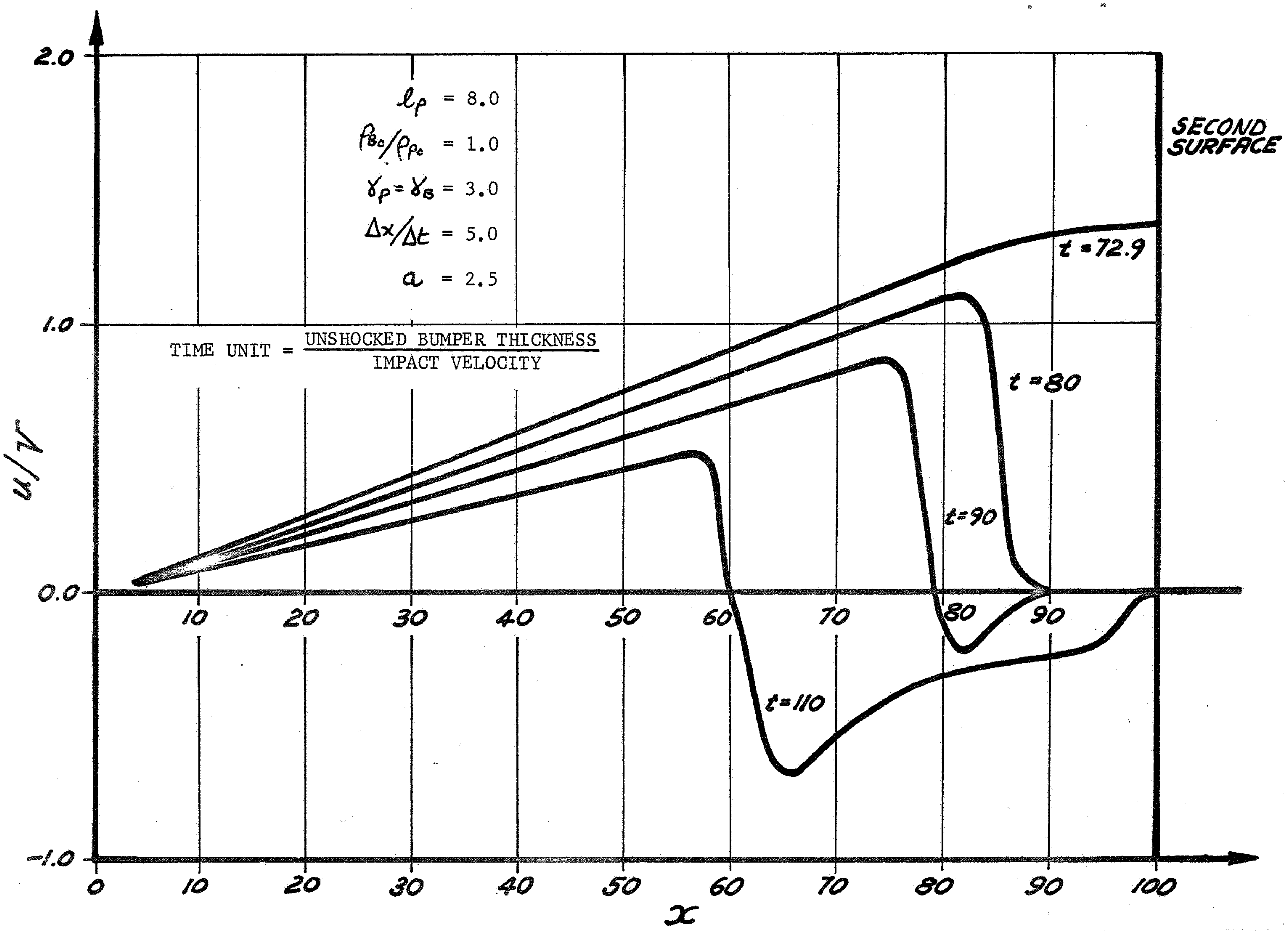

Fig. 2.9 Non-Dimensional Velocity Profiles for Interaction of the Gas Cloud with a Secondary Plate 100 Bumper Thicknesses Downstream

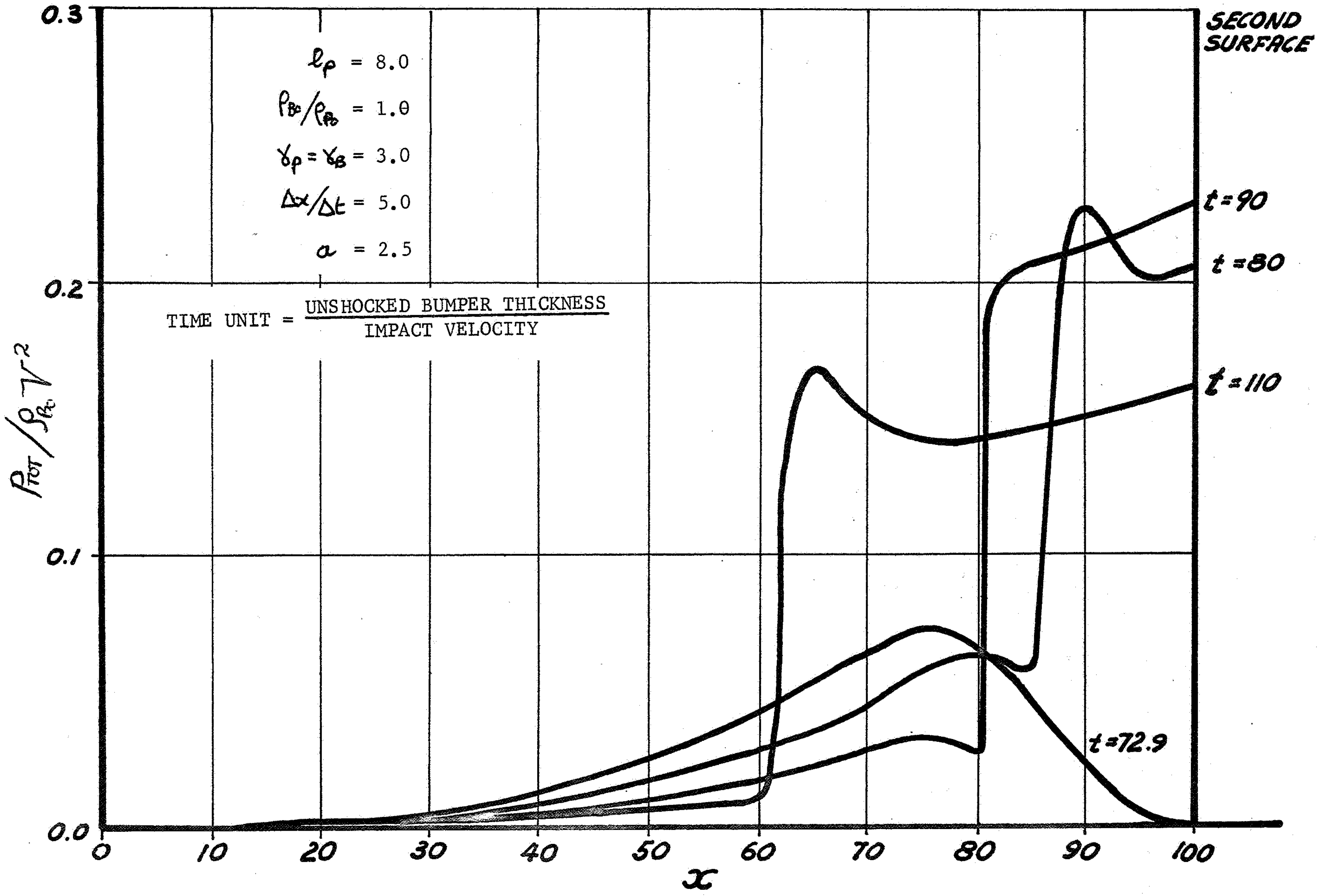

Fig. 2.10 Profiles of Non-Dimensional Total Pressure for Interaction of the Gas Cloud with a Secondary Surface 100 Bumper Thicknesses Downstream

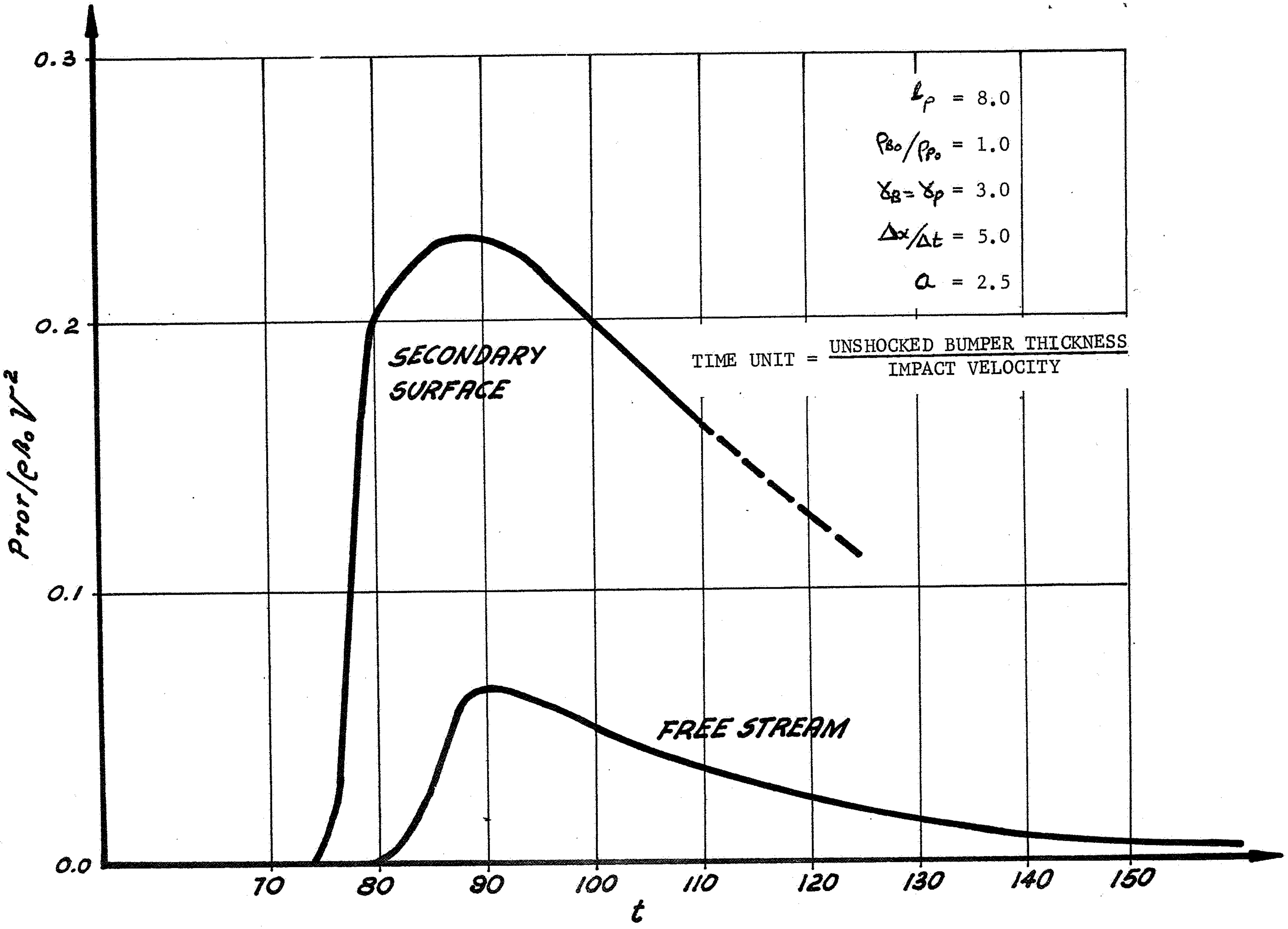

Fig. 2.11 Non-Dimensional Total Pressure vs. Time 100 Bumper Thicknesses Downstream for Free Flow and Secondary Surface Cases

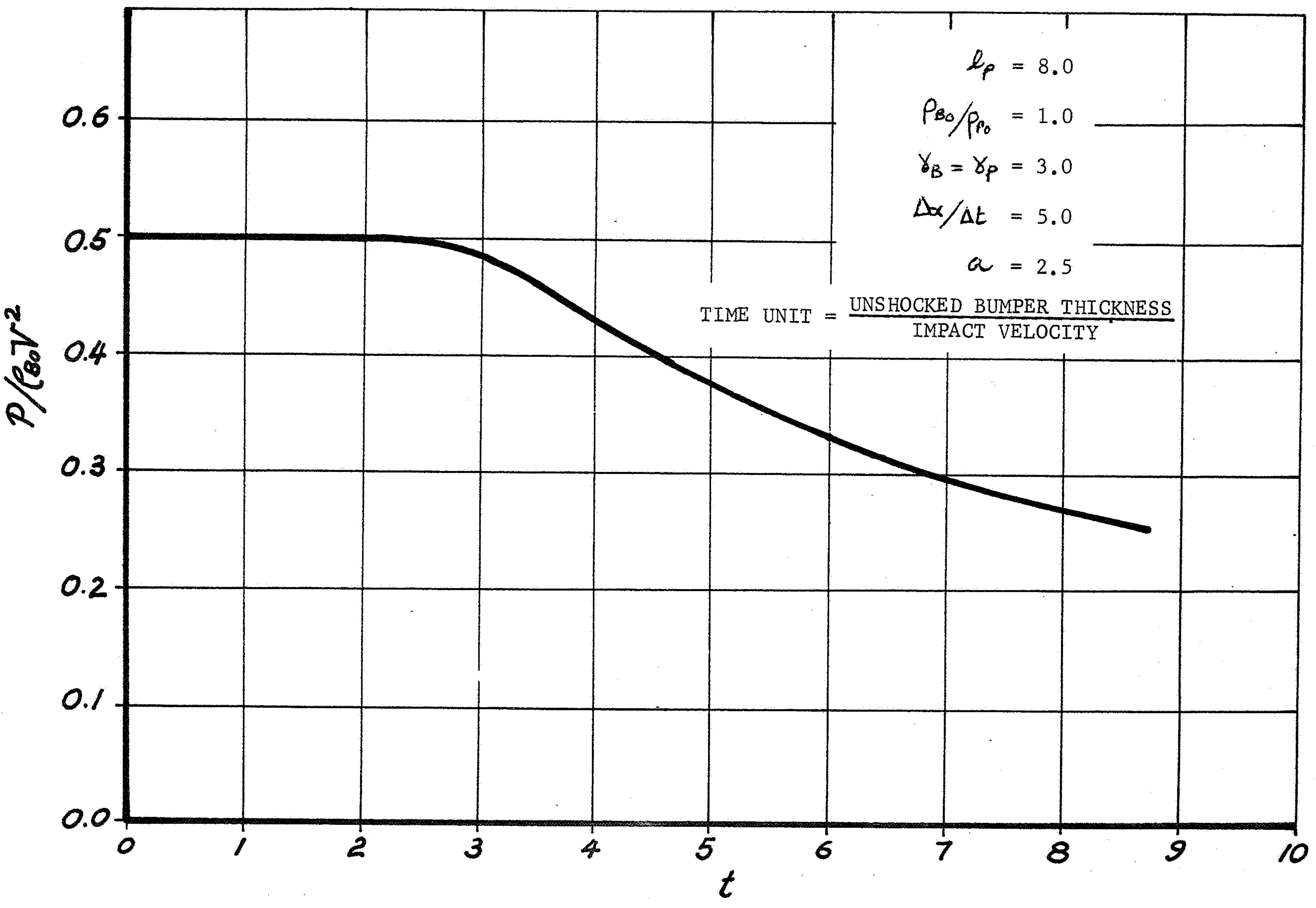

Fig. 2.12 Non-Dimensional Pressure behind the Pellet Shock vs. Time

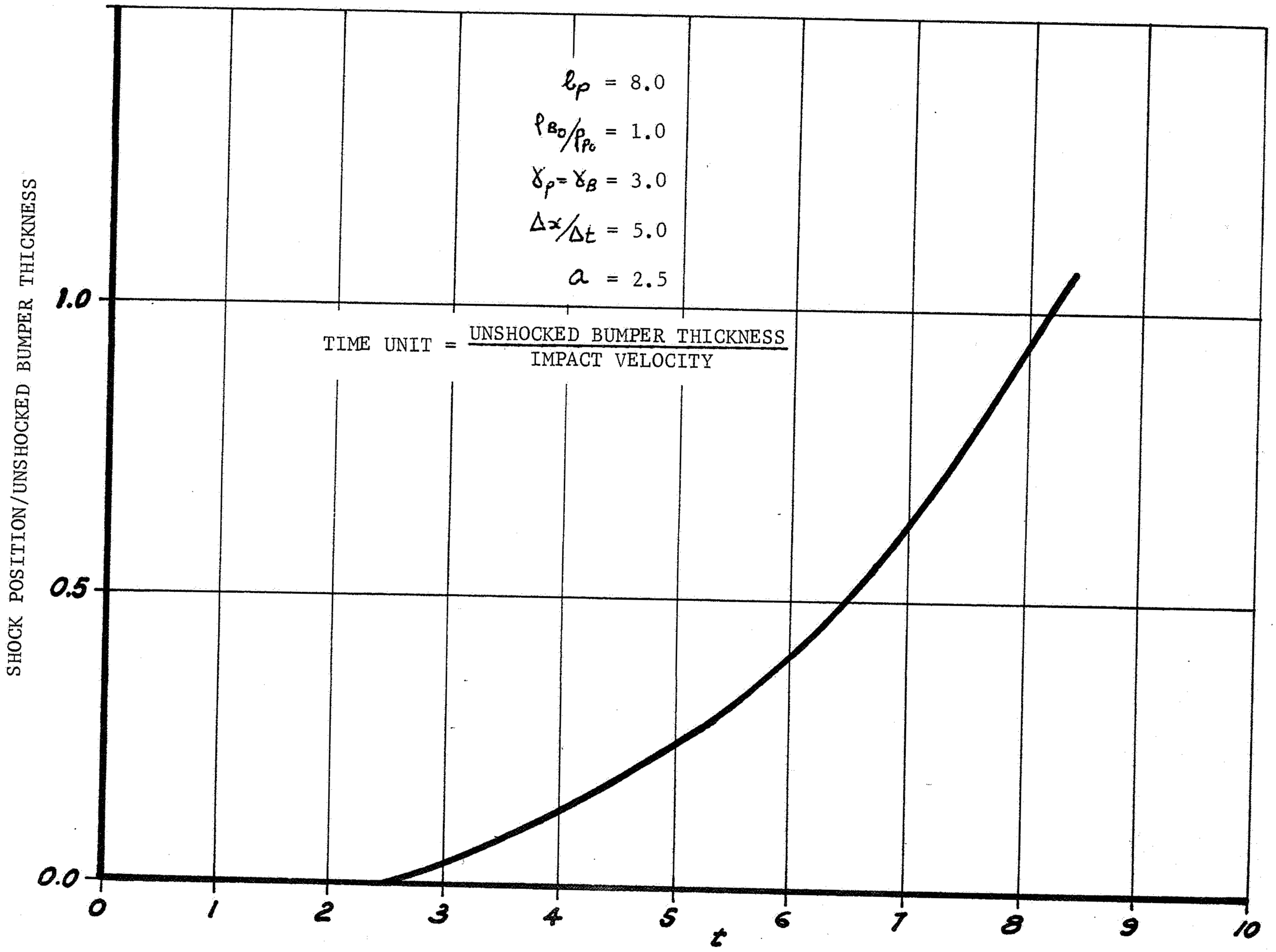

Fig. 2.13 Position of the Pellet Shock vs. Time

REFERENCES

1. Bull, G.V.

   "On the Impact of Pellets with Thin Plates"
   McGill University
   T.N. 1-10/61 (1961)

2. Courant & Friedrichs

   "Supersonic Flow & Shock Waves"
   Interscience (1948)

3. Shanfield, Lee and Bach

   "A Finite-Difference Solution for the Cylindrical Expansion of a Gas Cloud into a Vacuum"
   NASA CR-54254 (March 1965)

4. Greenspan, M.P. and Butler, D.S.

   "On the Expansion of a Gas into a Vacuum"
   Journal of Fluid Mechanics, Vol. 13 Part I
   (May 1962)

5. Copson, E.T.

   "The Expansion of a Gas Cloud into a Vacuum"
   Monthly Notices of the Royal Astronomical Society
   Vol. 110

6. Von Neumann, J. and Richtmyer, R.D.

   "A method for the numerical calculations of hydrodynamical shocks"
   Journal of Applied Physics, Vol. 21, p. 232 (1950)

7. Richtmyer, R.D.

   "Difference Methods for Initial-Value Problems"
   Interscience Publishers, Inc. (New York)

8. Richtmyer, R.D.

   "A Survey of Difference Methods for Non-Steady Fluid Dynamics"
   National Center for Atmospheric Research, Boulder, Colorado 80301
   NCAR Technical Notes 63-2

9. Shuman, F.G.

   "Numerical Methods in Weather Prediction: II. Smoothing and Filtering"
   Monthly Weather Review (November 1957)

REFERENCES (cont'd)

10. Friend, W.H. et. al.

"An Investigation of Explosive Oxidations Initiated by Hypervelocity Impacts"
AFFDL-TR-67-92 (May 1967)

APPENDIX A

Stability of the Isentropic Scheme

We had (2.1.5), (2.1.6):

$$c_j^{n+1} = \frac{1}{2}\left(c_{j+1}^n + c_{j-1}^n\right) - \frac{\gamma - 1}{2}\,\frac{\Delta t}{\Delta x}\left(c_j^n\,\frac{u_{j+1}^n - u_{j-1}^n}{2} + \frac{2u_j^n}{\gamma - 1}\,\frac{c_{j+1}^n - c_{j-1}^n}{2}\right) \tag{A.1}$$

$$u_j^{n+1} = \frac{1}{2}\left(u_{j+1}^n + u_{j-1}^n\right) - \frac{\Delta t}{\Delta x}\left(u_j^n\,\frac{u_{j+1}^n - u_{j-1}^n}{2} + \frac{2c_j^n}{\gamma - 1}\,\frac{c_{j+1}^n - c_{j-1}^n}{2}\right) \tag{A.2}$$

We take stability of a system of finite difference equations to mean stability of the corresponding set of linearized equations. For (A.1), (A.2) we have, on substituting a local perturbation and dropping subscripts on the zero order terms:

$$c_j^{n+1} = \frac{1}{2}\left(c_{j+1}^n + c_{j-1}^n\right) - \frac{\gamma -1}{2}\,\frac{\Delta t}{\Delta x}\left(c\,\frac{u_{j+1}^n - u_{j-1}^n}{2} + \frac{2u}{\gamma - 1}\,\frac{c_{j+1}^n - c_{j-1}^n}{2}\right) \tag{A.3}$$

$$u_j^{n+1} = \frac{1}{2}\left(u_{j+1}^n + u_{j-1}^n\right) - \frac{\Delta t}{\Delta x}\left(u\,\frac{u_{j+1}^n - u_{j-1}^n}{2} + \frac{2c}{\gamma - 1}\,\frac{c_{j+1}^n - c_{j-1}^n}{2}\right) \tag{A.4}$$

One now assumes a Fourier space dependence for the perturbation:

$$\xi_j^n = \xi^n \exp(ikj\Delta x)$$

Then (A.3), (A.4) become:

$$c^{n+1} = c^n (\cos(k\Delta x) - iul\sin(k\Delta x)) - (\frac{\gamma-1}{2} icl\sin(k\Delta x))\, u^n \qquad \text{A.5}$$

$$u^{n+1} = u^n (\cos(k\Delta x) - iul\sin(k\Delta x)) - (\frac{2}{\gamma-1} icl\sin(k\Delta x))\, c^n \qquad \text{A.6}$$

where $l = \frac{\Delta t}{\Delta x}$

i.e.
$$\begin{pmatrix} c^{n+1} \\ u^{n+1} \end{pmatrix} = \begin{pmatrix} \cos(k\Delta x) - iul\sin(k\Delta x) & -\frac{\gamma-1}{2} icl\sin(k\Delta x) \\ -\frac{2}{\gamma-1} icl\sin(k\Delta x) & \cos(k\Delta x) - iul\sin(k\Delta x) \end{pmatrix} \begin{pmatrix} c^n \\ u^n \end{pmatrix} \qquad \text{A.7}$$

The matrix on the right hand side of (A.7), which takes the state at time $n\Delta t$ into that at $(n + 1)\Delta t$, is called the amplification matrix, G. The Von Neumann necessary condition for stability (7) may be written as:

$$\max_i |\lambda_i| \leq 1 + 0(\Delta t) \qquad \text{A.8}$$

where λ_i are the eigenvalues of G, $i = 1,2, \ldots n$

For the case at hand we have:

$$\det |G - \lambda I| = \begin{vmatrix} \cos(k\Delta x) - iul\sin(k\Delta x) - \lambda & -\frac{\gamma-1}{2} icl\sin(k\Delta x) \\ -\frac{2icl}{\gamma-1}\sin(k\Delta x) & \cos(k\Delta x) - iul\sin(k\Delta x) - \lambda \end{vmatrix} = 0$$

$$\therefore \quad \lambda = \cos(k\Delta x) - i \sin(k\Delta x) \quad (ul \pm cl)$$

Hence $\quad |\lambda| \leq 1 + 0\ (\Delta t) \quad$ reduces to

$$(u \pm c)1 \leq 1 + 0\ (\Delta t)$$

In practice one uses the form:

$$\frac{\Delta x}{\Delta t} \geq u \pm c \qquad \text{A.9}$$

(A.9) is usually referred to as the stability condition for (A.1), (A.2).

APPENDIX B

Stability of the Non-Isentropic Equations

We had (2.2.5)

$$\frac{\rho_j^{n+1}-\rho_j^n}{\Delta t} + u_j^{n+1}\frac{\rho_j^n-\rho_{j-1}^n}{\Delta x} = -\rho_j^n\frac{u_{j+1}^{n+1}-u_{j-1}^{n+1}}{2\Delta x}, \quad u_j^{n+1}\geq 0 \qquad \text{B.1}$$

$$\frac{u_j^{n+1}-u_j^n}{\Delta t} + u_j^n\frac{u_j^n-u_{j-1}^n}{\Delta x} = -\frac{1}{\rho_j^n}\frac{p_{j+1}^n-p_{j-1}^n}{2\Delta x}, \quad u_j^n\geq 0 \qquad \text{B.2}$$

$$\frac{\varepsilon_j^{n+1}-\varepsilon_j^n}{\Delta t} + u_j^{n+1}\frac{\varepsilon_j^n-\varepsilon_{j-1}^n}{\Delta x} = -\frac{p_j^n}{\rho_j^n}\frac{u_{j+1}^{n+1}-u_{j-1}^{n+1}}{2\Delta x}, \quad u_j^{n+1}\geq 0 \qquad \text{B.3}$$

As in Appendix A, we proceed to obtain linearized equations. (B.1) and (B.2) may be immediately rewritten as:

$$\rho_j^{n+1} + \frac{\rho_1}{2}\left(u_{j+1}^{n+1}-u_{j-1}^{n+1}\right) = \rho_j^n - \frac{u_1}{2}\left(\rho_{j+1}^n-\rho_j^n\right) \qquad \text{B.4}$$

$$u_j^{u+1} = u_j^n - \frac{u_1}{2}\left(u_{j+1}^n-u_{j-1}^n\right) - \frac{1}{2\rho}\left(p_{j+1}^n-p_{j-1}^n\right) \qquad \text{B.5}$$

(B.3) is linearized and somewhat recasted by noting:

$$\varepsilon = F(p,\rho)$$

$$\frac{\partial\varepsilon}{\partial t} = F_p\frac{\partial p}{\partial t} + F_\rho\frac{\partial\rho}{\partial t}$$

$$\frac{\partial\varepsilon}{\partial x} = F_p\frac{\partial p}{\partial x} + F_\rho\frac{\partial\rho}{\partial x}$$

Hence (B.3) becomes:

$$p_j^{n+1} + \frac{lp}{2\rho F_p} (u_{j-1}^{n+1} - u_{j-1}^{n+1}) + \frac{F_\rho}{F_p} \left(\rho_j^{n+1} - \rho_j^n + \frac{ul}{2} (\rho_{j+1}^n - \rho_{j-1}^n) \right) = p_j^n - \frac{ul}{2} (p_{j+1}^n - p_{j-1}^n)$$

Substituting from (B.4) this becomes:

$$p_j^{n+1} + l \frac{p - \rho^2 F_\rho}{2\rho F_p} (u_{j+1}^{n+1} - u_{j-1}^{n+1}) = p_j^n - \frac{ul}{2} (p_{j+1}^n - p_{j-1}^n) \qquad \text{B.6}$$

Note that for isentropic variations

$$d\varepsilon = -pd\,(1/\rho)$$

i.e. $\quad F_p dp + F_\rho d\rho - \frac{p}{\rho^2} d\rho = 0$

The isentropic sound speed, c is the square root of $\left(\frac{dp}{d\rho}\right)$ along an adiabat. Hence

$$c^2 = \frac{\frac{p}{\rho^2} - F_\rho}{F_p}$$

Thus (B.6) may be written

$$p_j^{n+1} + \frac{lc^2\rho}{2} (u_{j+1}^{n+1} - u_{j-1}^{n+1}) = p_j^n - \frac{ul}{2} (p_{j+1}^n - p_{j-1}^n) \qquad \text{B.7}$$

We now substitute a Fourier spatial dependence into (B.4), (B.5), and (B.7) to obtain:

$$\left.\begin{aligned} &\rho^{n+1} + iB\rho l u^{n+1} = \rho^n A \\ &u^{n+1} = Au^n - i \frac{Bl}{\rho} p^n \\ &p^{n+1} + \rho l c^2 iBu^{n+1} = p^n A \end{aligned}\right\} \qquad \text{B.8}$$

where $$\xi^n = \xi_j^n \exp(-ikj\Delta x)$$

$$B = \sin(k\Delta x) \qquad \text{B.9}$$

$$A = 1 + ul(e^{-ik\Delta x} - 1)$$

The amplification matrix, G is given by

$$G = \begin{pmatrix} A & -B^2l^2 & -i\,AB\rho\,l \\ 0 & A-(Bcl)^2 & -ABi\rho\,c^2l \\ 0 & -i\frac{Bl}{\rho} & A \end{pmatrix} \qquad \text{B.10}$$

G has characteristic equation:

$$(A-\lambda)\,((A-\lambda)(A-(Bcl)^2-\lambda)+AB^2c^2l^2) = 0$$

The first eigenvalue may be written down immediately:

$$\lambda_1 = A = 1 + ul\,(e^{-ik\Delta x} - 1) \qquad \text{B.11}$$

Hence $$|\lambda| \leq 1 \qquad \text{if } 0 \leq u\frac{\Delta t}{\Delta x} \leq 1 \qquad \text{B.12}$$

The other two eigenvalues are the roots of the quadratic equation

$$\lambda^2 + \lambda((Bcl)^2 - 2A) + A^2 = 0 \qquad \text{B.13}$$

We now ask under what conditions one of the roots of (B.13) may have amplitude unity.

If $\sin(k\Delta x) = 0$ we have from (B.9), (B.13)

$$\lambda_1 = \lambda_2 = \lambda_3 = A$$

and since in this case A = 1, no additional requirement is necessary.

Otherwise:

$$\lambda = A - \frac{B^2c^2l^2}{2} \pm Bcl\sqrt{\frac{B^2c^2l^2}{4} - A}$$

$$= -\left(\frac{Bcl}{2} \mp \sqrt{K}\right)^2 \qquad \text{B.14}$$

$$\text{where} \quad K = \frac{B^2c^2l^2}{4} - A \qquad \text{B.15}$$

We may write out A in terms of B as:

$$A = 1 - \frac{ulB^2}{2} \pm i\frac{ulB}{2}(4 - B^2)^{\frac{1}{2}}$$

Whence we have K:

$$K = \frac{B^2c^2l^2}{4} - 1 + \frac{ulB^2}{2} \mp i\frac{ulB}{2}(4 - B^2)^{\frac{1}{2}} \qquad \text{B.16}$$

The requirement that one of the roots of (B.13) lie on the unit circle may be written as:

$$e^{i\theta} = \frac{Bcl}{2} \pm \sqrt{K} \qquad \text{with } \theta \text{ real}$$

Substituting from B.16 one has

$$e^{2i\theta} - Bcle^{i\theta} + \frac{B^2c^2l^2}{4} = \frac{B^2c^2l^2}{4} - 1 + \frac{ulB^2}{2} \mp i\frac{ulB}{2}(4 - B^2)^{\frac{1}{2}}$$

Separating the above into real and imaginary parts:

$$\cos 2\theta = Bcl\cos\theta - 1 + \frac{ulB^2}{2} \qquad \text{B.17}$$

$$\sin 2\theta = Bcl\sin\theta \mp \frac{ulB}{2}\sqrt{4 - B^2} \qquad \text{B.18}$$

We now eliminate θ from (B.17), (B.18) to produce a compatability relation. This will produce the desired result. (B.17) yields:

$$\cos\theta = \frac{Bcl}{4} \pm \frac{B}{4}\sqrt{c^2l^2 + 4ul} \qquad \text{B.19}$$

whence

$$\sin\theta = \left(1 - \frac{B^2ul}{4} - \frac{B^2c^2l^2}{8} \mp \frac{B^2cl}{8}\sqrt{c^2l^2 + 4ul} \right)^{\frac{1}{2}} \qquad \text{B.20}$$

We now substitute (B.19), (B.20) into (B.18) to obtain

$$\left\{ 1 - \frac{B^2ul}{4} - \frac{B^2c^2l^2}{8} \mp \frac{B^2cl\Gamma}{8} \right\}\left\{ \frac{Bcl}{2} \pm \frac{B}{2}\Gamma - \frac{Bcl}{2} \right\}^2$$

$$= u^2l^2B^2 - \frac{u^2l^2B^4}{4}$$

where we have used $\Gamma = \sqrt{c^2l^2 + 4ul}$.

The above equation reduces to

$$4c^2l^2\Gamma^2 = (2c^2l^2 + 4ul - 4u^2l^2)^2$$

or

$$c^2l^2 = (1 - ul)^2$$

which we recognize to be the condition

$$\pm (u \pm c)l = 1$$

Consequently a root of (B.13) will have amplitude unity if

(i) $\sin(k\Delta x) = 0$ B.21

or (ii) $\pm (u \pm c)l = 1$

Now note that the eigenvalues of G are continuous functions of u, c, l, k, and if $\sin(k\Delta x) \neq 0$, $c = 0$ and $0 < ul < 1$, then from (B.21)

$$\lambda_1 = \lambda_2 = \lambda_3 = A \quad \text{with} \quad |A| < 1$$

We then assert that by continuity, the eigenvalues cannot be outside the unit circle for $(u + c)1 \leq 1$. (The signs have been dropped since c is always non-negative and u has been assumed non-negative.) Suppose λ_2, say, were outside the unit circle with $(u + c)\ 1 \leq 1$; then letting $c \rightarrow o$ would cause $\lambda_2 \longrightarrow A$, inside the unit circle. Hence, by continuity, λ_2 would be on the unit circle for some value of c for which

$$(u + c)1 < 1$$

which would violate (B.20).

If $u < o$, forward space differences are required in the convective terms $u \frac{\partial}{\partial x}$ in (B.1) to (B.3). Then the transformations $x \rightarrow (-x)$ and $u \rightarrow (-u)$ will bring us back to the original equations. Thus the condition for stability is taken to be

$$(|u| + c) \frac{\Delta t}{\Delta x} \leq 1 \quad .$$

APPENDIX C

Stability of the Non-Isentropic Equations with Artificial Viscosity

We had (2.3.7), (2.3.8):

$$\frac{\rho_j^{n+1} - \rho_j^n}{\Delta t} + u_j^{n+1} \frac{\rho_j^n - \rho_{j-1}^n}{\Delta x} = - \rho_j^n \frac{u_{j+1}^{n+1} - u_{j-1}^{n+1}}{2 \Delta x} ,$$

$$u_j^{n+1} \geq 0 \qquad \text{C.1}$$

$$\frac{u_j^{n+1} - u_j^n}{\Delta t} + u_j^n \frac{u_j^n - u_{j-1}^n}{\Delta x} = - \frac{1}{\rho_j^n} \frac{p_{j+1}^n + q_{j+1}^n - p_{j-1}^n - q_{j-1}^n}{2 \Delta x} ,$$

$$u_j^n \geq 0 \qquad \text{C.2}$$

$$\frac{\varepsilon_j^{n+1} - \varepsilon_j^n}{\Delta t} + u_j^{n+1} \frac{\varepsilon_j^n - \varepsilon_{j-1}^n}{\Delta x} = \frac{-p_j^n + q^n}{\rho_j^n} \frac{u_{j+1}^{n+1} - u_{j-1}^{n+1}}{2 \Delta x} ,$$

$$u_j^{n+1} \geq 0 \qquad \text{C.3}$$

$$q_j^n = \begin{cases} \frac{1}{8} a^2 (\rho_j^n + \rho_j^{n-1})(u_{j+1}^n - u_{j-1}^n)^2 & \text{if } u_{j+1}^n - u_j^n < 0 \\ 0 & \text{if } u_{j+1}^n - u_j^n \geq 0 \end{cases} \qquad \text{C.4}$$

where $l_v = a \Delta x$.

The linearization proceeds as in Appendix B, but we consider q as being an independent variable. Consequently we have:

$$\rho_j^{n+1} - \rho_j^n + u \frac{\Delta t}{\Delta x} (\rho_j^n - \rho_{j-1}^n) = - \rho \frac{\Delta t}{2 \Delta x} (u_{j+1}^{n+1} - u_{j-1}^{n+1}) \qquad \text{C.5}$$

$$u_j^{n+1} - u_j^n + u\frac{\Delta t}{\Delta x}(u_j^n - u_{j-1}^n) = \frac{-\Delta t}{2\rho\Delta x}(p_{j+1}^n + q_{j+1}^n - p_{j-1}^n - q_{j-1}^n) \qquad \text{C.6}$$

$$\mathcal{E}_j^{n+1} - \mathcal{E}_j^n + u\frac{\Delta t}{\Delta x}(\mathcal{E}_j^n - \mathcal{E}_{j-1}^n) = -\frac{(p+q)}{2\rho}\frac{\Delta t}{\Delta x}(u_{j+1}^{n+1} - u_{j-1}^{n+1}) \qquad \text{C.7}$$

The first order equation for q is derived from (C.4) under the assumption that the perturbance is dominated by the error in the representation of the derivative. We regard $(\rho\frac{\partial u}{\partial x})$ as a zero order quantity and write

$$q_j^{n+1} = \frac{2l_2}{\Delta x}\left(\rho\frac{\partial u}{\partial x}\right)(u_{j+1}^{n+1} - u_{j-1}^{n+1}) \qquad \text{C.8}$$

(One may carry through the calculation with the added term $\rho_j^{n+1}\, l_2 \left(\frac{\partial u}{\partial x}\right)^2$. However, it turns out to have negligible effect, justifying the a priori assumption.)

With the abbreviations

$$B = \sin(k\Delta x)$$

$$A = 1 + u\frac{\Delta t}{\Delta x}(e^{-ik\Delta x} - 1)$$

$$c^* = \left(\frac{p+q}{\rho^2} - \frac{\partial\mathcal{E}}{\partial\rho}\right) \Big/ \frac{\partial\mathcal{E}}{\partial p} \qquad \text{C.9}$$

$$\Lambda = 2l_v\rho\frac{\partial u}{\partial x}$$

one has, on substituting a Fourier spatial dependence into (C.5) to (C.8):

$$\rho^{n+1} = \rho^n A - i\rho\frac{\Delta t}{\Delta x}B\left(u^n A - \frac{i}{\rho}\frac{\Delta t}{\Delta x}B(p^n + q^n)\right) \qquad \text{C.10}$$

$$u^{n+1} = u^n A - \frac{i}{\rho}\frac{\Delta t}{\Delta x}B(p^n + q^n) \qquad \text{C.11}$$

$$p^{n+1} = p^n A - i \frac{\Delta t}{\Delta x} \rho c^* B \left(u^n A - \frac{i}{\rho} \frac{\Delta t}{\Delta x} B (p^n + q^n)\right) \qquad \text{C.12}$$

$$q^{n+1} = \frac{\Lambda iB}{\Delta x} \left(u^n - \frac{i \Delta t}{\rho \Delta x} B (p^n + q^n)\right) \qquad \text{C.13}$$

One may write the fourth order amplification matrix G as:

$$G = \begin{pmatrix} A & -i \rho \frac{\Delta t}{\Delta x} AB & - \frac{(\Delta t)^2}{(\Delta x)^2} B^2 & - \frac{(\Delta t)^2}{(\Delta x)^2} B^2 \\ 0 & A & - \frac{i}{\rho} \frac{\Delta t}{\Delta x} B & - \frac{i}{\rho} \frac{\Delta t}{\Delta x} B \\ 0 & - i \frac{\Delta t}{\Delta x} \rho c^* AB & A - \frac{(\Delta t)^2}{(\Delta x)^2} c^* B^2 & - \frac{(\Delta t)^2}{(\Delta x)^2} c^* B^2 \\ 0 & \frac{\Lambda iB}{\Delta x} A & \frac{\Lambda iB}{\Delta x} \left(- \frac{i}{\rho} \frac{\Delta t}{\Delta x} B\right) & \frac{\Lambda iB}{\Delta x} \left(- \frac{i}{\rho} \frac{\Delta t}{\Delta x} B\right) \end{pmatrix}$$

The eigenvalue equation for G is

$$\begin{vmatrix} A - \lambda & - i \rho \frac{\Delta t}{\Delta x} AB & - \frac{(\Delta t)^2}{(\Delta x)^2} B^2 & - \frac{(\Delta t)^2}{(\Delta x)^2} B^2 \\ 0 & A - \lambda & - \frac{i}{\rho} \frac{\Delta t}{\Delta x} B & - \frac{i}{\rho} \frac{\Delta t}{\Delta x} B \\ 0 & - i \frac{\Delta t}{\Delta x} \rho c^* AB & A - \frac{(\Delta t)^2}{(\Delta x)^2} c^* B^2 - \lambda & - \frac{(\Delta t)^2}{(\Delta x)^2} c^* B^2 \\ 0 & \frac{\Lambda iB}{\Delta x} A & \frac{\Lambda iB}{\Delta x} \left(- \frac{i}{\rho} \frac{\Delta t}{\Delta x} B\right) & \frac{\Lambda iB}{\Delta x} \left(- \frac{i}{\rho} \frac{t}{x} B\right) - \lambda \end{vmatrix} = 0$$

Evidently the first eigenvalue is

$$\lambda_1 = A \qquad \text{C.14}$$

Then dividing the fourth row by $\frac{\Lambda iB}{\Delta x}$ and subtracting it from the second, one has for the remaining three eigenvalues:

$$\begin{vmatrix} -\lambda & 0 & \frac{\lambda\Delta x}{iB} \\ \frac{\Lambda iB}{\Delta x} - i\frac{\Delta t}{\Delta x}\rho c^{*}AB & A - \frac{(\Delta t)^2}{(\Delta x)^2}c^{*}B^2 - & -\frac{(\Delta t)^2}{(\Delta x)^2}c^{*}B^2 \\ \frac{\Lambda iAB}{\Delta x} & \frac{\Delta t}{\rho\Delta x}\frac{\Lambda}{\Delta x}B^2 & \frac{(\Delta t)}{(\Delta x)}\frac{\Lambda}{\Delta x}\frac{B^2}{\rho} - \lambda \end{vmatrix} = 0$$

Expanding in cofactors by the first row we get:

$$\lambda_2 = 0 \qquad \text{C.15}$$

while the last two eigenvalues satisfy the quadratic equation:

$$\left(A - \frac{(\Delta t)^2}{(\Delta x)^2} c^{*}B^2 - \lambda\right)\left(\frac{\Delta t}{\Delta x}\frac{\Lambda}{\Delta x}B^2 - \lambda + A\right) + \frac{\Delta t}{\Delta x}\frac{\Lambda B^2}{\rho\Delta x}\left(\frac{(\Delta t)^2}{(\Delta x)^2}c^{*}B^2 + \frac{\Delta t}{\Delta x}\frac{\Delta x}{\Lambda}\rho c^{*}A\right) = 0 \qquad \text{C.16}$$

We note that if $\Lambda = 0$, $c^{*} = c^2$ corresponding to the case of no viscosity, the above equation reduces to (B.13), as it should.

Rearranging (C.16) we have:

$$\lambda^2 + \lambda\left(\frac{(\Delta t)^2}{(\Delta x)^2}c^{*}B^2 - \frac{\Delta t}{\rho(\Delta x)^2}\Lambda B^2 - 2A\right) + A^2 + \frac{\Delta t}{\rho(\Delta x)^2}\Lambda AB^2 = 0 \qquad \text{C.17}$$

whence it is clear that for stability in the limit as Δt, Δx → 0 we will require

$$\frac{\Delta t}{(\Delta x)^2} \longrightarrow \text{finite constant} \qquad \text{C.18}$$

Hence letting $\Delta t, \Delta x \longrightarrow 0$ with (C.18) satisfied, (C.17) becomes:

$$\lambda^2 + \lambda \left(- \frac{\Delta t}{(\Delta x)^2} \frac{\Lambda_B^2}{\rho} - 2 \right) + 1 + \frac{\Delta t}{(\Delta x)^2} \frac{\Lambda_B^2}{\rho} = 0$$

The roots of the quadratic equation are seen to be:

$$\lambda_3 = 1$$

$$\lambda_4 = 1 + \frac{\Delta t}{(\Delta x)^2} \cdot 2l_v \left(\frac{\partial u}{\partial x} \right) \sin^2 (k \Delta x)$$

Hence to satisfy the Von Neumann necessary condition we require:

$$- \frac{\Delta t}{(\Delta x)^2} \cdot 2l_v \frac{\partial u}{\partial x} \leq 2 \qquad \text{C.19}$$

since $\frac{\partial u}{\partial x} \leq 0$ in the shock transition zone.

As an estimate of $\frac{\partial u}{\partial x}$ we naturally take the extreme value predicted by equation (1.5.5). One may then write (C.19) with the help of (1.5.5) as:

$$\frac{\Delta t}{\Delta x} \left(a \, (u_2 - u_1) \sqrt{\frac{\gamma + 1}{2}} \right) \leq 1 \qquad \text{C.20}$$

In order to compare this with the usual form for the stability condition we assume the most stringent case, namely a strong shock, so that:

$$\frac{\rho_2}{\rho_1} = \frac{\gamma + 1}{\gamma - 1} \quad \text{and} \quad p_1 = 0 \qquad \text{C.21}$$

From the conservation of mass and momentum:

$$\rho_1 \, (D - u_1) = \rho_2 \, (D - u_2) \qquad \text{C.22}$$

$$p_1 + \rho_1 (D - u_1)^2 = p_2 + \rho_2 (D - u_2)^2 \qquad \text{C.23}$$

Together with (C.21) one obtains

$$D - u_2 = \sqrt{\frac{\gamma - 1}{2}} \quad c_2 \qquad \text{C.24}$$

where $c_2 = \sqrt{\frac{\gamma p_2}{\rho_2}}$ is the isentropic sound speed in the shocked gas. Similarly one finds:

$$D - u_1 = \sqrt{\frac{(\gamma + 1)^2}{2\gamma(\gamma - 1)}} \qquad \text{C.25}$$

Hence from (C.24) and (C.25) one has:

$$u_2 - u_1 = c_2 \sqrt{\frac{2}{\gamma(\gamma - 1)}} \qquad \text{C.26}$$

Consequently we write the stability condition (C.20) in the extreme case as:

$$\frac{\Delta t}{\Delta x} \, a c_2 \sqrt{\frac{\gamma + 1}{\gamma(\gamma - 1)}} \leq 1 \qquad \text{C.27}$$

DISTRIBUTION LIST

National Aeronautics and Space Administration
Lewis Research Center
21000 Brookpark Road
Cleveland, Ohio 44135

		COPIES
Attention:	Contracting Officer, MS 500-210	1
	Liquid Rocket Technology Branch, MS 500-209	8
	Technical Report Control Office, MS 5-5	1
	Technology Utilization Office, MS 3-16	1
	AFSC Liaison Office, MS 4-1	2
	J.F. Mondt, MS 500-309	1
	Library, MS 60-3	2
	Robert Johns, MS 49-1	1
	Office of Reliability & Quality Assurance, MS 500-203	1
	D.L. Nored, MS 500-209	1
	E.W. Conrad, MS 100-1	1
	W.E. Roberts, MS 3-17	1
	F.S. Stepka, MS 49-1	1

National Aeronautics and Space Administration
Washington, D.C. 20546

Attention:	Code MT	1
	RPX	2
	RPL	2
	SV	1
	RV-2	2

Scientific and Technical Information Facility
P.O. Box 33
College Park, Maryland 20740

Attention:	NASA Representative Code CRT	6

National Aeronautics and Space Administration
Ames Research Center
Moffett Field, California 94035

Attention:	Library	1
	C.A. Syvertson	1
	C. Robert Nysmith	1
	James Summers	1

	COPIES
National Aeronautics and Space Administration Flight Research Center P.O. Box 273 Edwards, California 93523	
Attention: Library	1
National Aeronautics and Space Administration Goddard Space Flight Center Greenbelt, Maryland 20771	
Attention: Library	1
Code 250	1
National Aeronautics and Space Administration John F. Kennedy Space Center Cocoa Beach, Florida 32931	
Attention: Library	1
National Aeronautics and Space Administration Langley Research Center Langley Station Hampton, Virginia 23365	
Attention: Library	1
Mr. D. Davis, Jr.	1
Mr. Richard Heldenfels	1
Mr. William Kinard	1
Mr. Edwin Kauszewski, Mail Stop 188	1
National Aeronautics and Space Administration Manned Spacecraft Center Houston, Texas 77001	
Attention: Library	1
Lockheed Missiles & Space Company P.O. Box 504 Sunnyvale, California	
Attention: Technical Information Center	1

	COPIES
National Aeronautics and Space Administration George C. Marshall Space Flight Center Huntsville, Alabama 35812	
Attention: Tech. Documents Library	1
Keith Chandler, R-P&VE-PA	1
Research Projects Div. (M-RP-R)	1
James W. Carter, Future Projects Office, MFPO	1
Jet Propulsion Laboratory 4800 Oak Grove Drive Pasadena, California 91103	
Attention: Library	1
Earl E. Newham, Reports Group	2
Dr. V. Jaffe	1
University of California Los Alamos Scientific Lab. P.O. Box 1663 Los Alamos, New Mexico	1
Defense Documentation Center Cameron Station Alexandria, Virginia 22314	1
RTD(RTNP) Bolling Air Force Base Washington, D.C. 20332	1
Attention: J.W. Minette	1
E.A. Kritzer	1
Aeronautical Systems Division Air Force Systems Command Wright-Patterson Air Force Base Dayton, Ohio	
Attention: D.L. Schmidt, Code ASRCNC-2	1
Lt. Lloyd Hedgepeth, ASRMFP-1	1
W.P. Conrardy, Chief, Applications Lab-Materials Control	1
Commander, Air Tech. Intelligence Center Attention: AFOIN-4B1A	2

COPIES

Air Force Systems Command
Andrews Air Force Base
Washington, D.C. 20332

Attention: Major R.L. Hayford 1

Professor Pei Chi Chou
Department Mechanical Engineering
Drexel Institute of Technology
Philadelphia, Pennsylvania 1

Ballistic Research Laboratory
Aberdeen, Maryland

Attention: Floyd E. Allison 1
Robert J. Eichelberger 1

Commander
U.S. Naval Missile Center
Point Mugu, California 93041

Attention: Technical Library 1

Computing Devices of Canada Limited
P.O. Box 508
Ottawa 4, Canada

Attention: Dr. G.P.T. Wilenius 1

Director
U.S. Naval Research Laboratory
Washington, D.C. 20390

Attention: Walter W. Atkins 1
Mario A. Persechino 1

Picatinny Arsenal
Dover, New Jersey

Attention: I. Forsten, Chief 1
Liquid Propulsion Laboratory

A.F. Cambridge Research Laboratory
Hascom Field, Mass.

Attention: Robert K. Soberman 1

		COPIES
Aerojet-General Corporation		
P.O. Box 296		
Azusa, California 91703		
Attention:	Librarian	1
Aerojet-General Corporation		
11711 South Woodruff Avenue		
Downey, California 90241		
Attention:	F.M. West, Chief Librarian	1
	J.F. Cullinane	1
Aerospace Corporation		
El Segundo, California		
Attention:	Robert Cooper	1
	Verne C. Frost	1
	Robert Herndon	1
	J. McClelland	1
	Milton Weiss	1
Aerospace Corporation		
San Bernardino, California		
Attention:	Rene B. Mortensen	1
	D.B. Singer	1
Arthur D. Little, Inc.		
Acorn Park		
Cambridge 40, Massachusetts		
Attention:	A.C. Tobey	1
	Dr. J.M. Bonneville	1
ARO, Incorporated		
Arnold Engineering Development Center		
Arnold AF Station, Tennessee 37389		
Attention:	Dr. B.H. Goethert	1
	Julius Lukasiewicz	1
AVCO Corporation		
Wilmington, Mass. 01887		
Attention:	Robert R. McMath/RAD	1

COPIES

Battelle Memorial Institute
505 King Avenue
Columbus, Ohio 43201

Attention: Report Library, Room 6A 1
R.E. Bowman/RAD/Effects Information Center 1

The Boeing Company
Aero Space Division
P.O. Box 3707
Seattle, Washington 98124

Attention: Library 1
Jack Lundeberg 1

Chance Vought Corporation Library
Box 5907
Dallas 22, Texas 1

Chemical Propulsion Information Agency
Applied Physics Laboratory
8621 Georgia Avenue
Silver Spring, Maryland 20910 1

Chrysler Corporation
Space Division
New Orleans, Louisiana

Attention: Librarian 1
Elayne M. Brower/AEB/2761 1

Cornell Aeronautical Lab., Inc.
Buffalo, N.Y.

Attention: Dr. William Rae 1

Douglas Aircraft Company, Inc.
Santa Monica Division
3000 Ocean Park Blvd.
Santa Monica, California 90405

Attention: C.W. Ferguson 1
H.H. Dixon 1

COPIES

Fundamental Methods Associates
31 Union Square West
New York 3, New York

Attention: Dr. Carl Klahr 1

Convair Division
General Dynamics Corporation
P.O. Box 1128
San Diego, California 92112

Attention: Library & Information Service (128-00) 2

General Electric Company
Re-Entry Systems Department
P.O. Box 8555
Philadelphia, Pennsylvania 19101

Attention: T.D. Riney/TEMO 1
J.F. Heyda/TEMO 1

General Motors Defense Research Labs
Santa Barbara, California

Attention: C.J. Maiden 1

Grumman Aircraft Engineering Corporation
Bethpage, Long Island, New York

Attention: Library, John Tlasmati 1

Harvard College Observatory
Cambridge, Massachusetts

Attention: Prof. F.L. Whipple 1

Lockheed Missiles and Space Company
Palo Alto, California

Attention: P.E. Sandorff 1

Lockheed Missiles & Space Company
Propulsion Engineering Division (D.55-11)
1111 Lockheed Way
Sunnyvale, California 94087

Attention: Library 1

	COPIES
Martin-Marietta Corporation Martin Division Baltimore 3, Maryland	
Attention: Science Technology Library (398)	1
Naval Ordnance Laboratory Maryland	
Attention: Arnold E. Seigel	1
Naval Ordnance Laboratory Corona, California	
Attention: Roy L. Nicholi	1
F.E. Winters, Jr.	1
New York University College of Engineering Research Division University Heights New York 53, New York	
Attention: Dr. Paul F. Winternite	1
North American Rockwell, Inc. Space & Information Systems Division 12214 Lakewood Boulevard Downey, California 90242	
Attention: Technical Information Center, D/096-722 (AJ01)	1
Allan J. Richardson, D/192 GB83	1
Northrop Space Laboratories 1001 East Broadway Hawthorne, California	
Attention: R.D. Johnson, Space Materials Lab.	1
Pennsylvania State University University Park, Pennsylvania	
Attention: Norman Davids	1

	COPIES
Republic Aviation Corporation Farmingdale, Long Island New York Attention: K. Singer, Space Systems Structures	1
Rocketdyne Division of North American Rockwell, Inc. 6633 Canoga Avenue Canoga Park, California 91304 Attention: Library, Department 596-306	1
Sandia Corporation Albuquerque, New Mexico Attention: Walter Herrmann	1
Stanford Research Institute 333 Ravenswood Avenue Menlo Park, California 94025 Attention: P.R. Gillette	1
Thiokol Chemical Corporation Reaction Motors Division Denville, New Jersey 07834 Attention: Librarian	1
TRW Systems Physical Research & Analysis Section P.O. 95001 Los Angeles 45, California	1
TRW Systems, Incorporated 1 Space Park Redondo Beach, California 90200 Attention: Library	1
United Aircraft Corporation Pratt & Whitney Division Florida Research & Development Center P.O. Box 2691 West Palm Beach, Florida 33402 Attention: Library	1

COPIES

University of Denver
Denver Research Institute
University Park
Denver, Colorado 80210

Attention: Rodney R. Recht, Mechanics Division 1

University of Toronto
Toronto, Canada

Attention: I.I. Glass 1

Utah Research and Development
2175 South 3270 West
Salt Lake City, Utah

Attention: Boyd Baugh 1

IIT Research Institute
Technology Center
Chicago, Illinois 60616

Attention: Dr. R.H. Cornish 1